

1 Regional uncertainty of GOSAT XCO₂ retrievals in China: 2 Quantification and attribution

3
4 Nian Bie^{1, 2}, Liping Lei¹, ZhaoCheng Zeng³, Bofeng Cai⁴, Shaoyuan Yang^{1, 2}, Zhonghua He^{1, 2},
5 Changjiang Wu^{1, 2}, and Ray Nassar⁵
6 ¹Key Laboratory of Digital Earth Science, Institute of Remote Sensing and Digital Earth, Chinese Academy of Sciences,
7 Beijing 100094, China
8 ²University of Chinese Academy of Sciences, Beijing 100049, China
9 ³Division of Geological and Planetary Sciences, California Institute of Technology, Pasadena, CA91125, USA
10 ⁴The Center for Climate Change and Environmental Policy, Chinese Academy for Environmental Planning, Ministry of
11 Environmental Protection, Beijing, 100012, China
12 ⁵Climate Research Division, Environment and Climate Change Canada, Canada

13 Correspondence to: leilp@radi.ac.cn

14 **Abstract.** The regional uncertainty of XCO₂ (column-averaged dry air mole fraction of CO₂) retrieved using different
15 algorithms from the Greenhouse gases Observing SATellite (GOSAT) and its attribution are still not well understood. This
16 paper investigates the regional performance of XCO₂ within a latitude band of 37°N~ 42°N segmented into 8 cells in a grid
17 of 5 ° from west to east (80°E ~120°E) in China, where there are typical land surface types and geographic conditions. The
18 former include the various land covers of desert, grassland and built-up areas mixed with cropland, and the latter include
19 anthropogenic emissions that change from small to large from west to east, including those from the megacity of Beijing. For
20 these specific cells, we evaluate the regional uncertainty of GOSAT XCO₂ retrievals by quantifying and attributing the
21 consistency of XCO₂ retrievals from four algorithms (ACOS, NIES, OCFP, and SRFP) by intercomparison. Particularly,
22 these retrievals are compared with simulated XCO₂ by the high-resolution nested model in East Asia of Goddard Earth
23 Observing System 3-D chemical transport model (GEOS-Chem). We introduce the anthropogenic CO₂ emissions data
24 generated from the investigation of surface emitting point sources that was conducted by the Ministry of Environmental
25 Protection of China to GEOS-Chem simulations of XCO₂ over the Chinese mainland. The results indicate that (1) regionally,
26 the four algorithms demonstrate smaller absolute biases of 0.7-1.1 ppm in eastern cells, which are covered by built-up areas
27 mixed with cropland with intensive anthropogenic emissions, than those in the western desert cells (1.0-1.6 ppm) with a
28 high-brightness surface from the pairwise comparison results of XCO₂ retrievals. The inconsistency of XCO₂ from the four
29 algorithms tends to be high in the Taklimakan Desert in western cells, which is likely induced by high surface albedo in
30 addition to dust aerosols in this region. (2) Compared with XCO₂ simulated by GEOS-Chem (GEOS-XCO₂), the XCO₂
31 values of ACOS and SRFP have better agreement with GEOS-XCO₂, while OCFP is the least consistent with GEOS-XCO₂.
32 (3) Viewing attributions of XCO₂ in the spatio-temporal pattern, ACOS and SRFP demonstrate similar patterns, while OCFP
33 is largely different from the others. In conclusion, the discrepancy in the four algorithms is the smallest in eastern cells in the
34 study area, where the megacity of Beijing is located and where there are strong anthropogenic CO₂ emissions, which implies

35 that XCO₂ from satellite observations could be reliably applied in the assessment of atmospheric CO₂ enhancements induced
36 by anthropogenic CO₂ emissions. The large inconsistency among the four algorithms presented in western deserts with a
37 high albedo and dust aerosols, moreover, demonstrates that further improvement is still necessary in such regions, even
38 though many algorithms have endeavored to minimize the effects of aerosols scattering and surface albedo.

39

40 Key words: GOSAT, XCO₂ retrieval algorithms, simulated XCO₂ by GEOS-Chem, regional uncertainty, anthropogenic
41 emissions, and desert

42 **1 Introduction**

43 The column-averaged dry air mole fraction of CO₂ (XCO₂) derived from satellite observations, such as the SCanning
44 Imaging Absorption spectroMeter of Atmospheric CHartography (SCIAMACHY) (Burrows et al., 1995; Bovensmann et al.,
45 1999), the Greenhouse gases Observing SATellite (GOSAT) (Yokoda et al., 2004), Orbiting Carbon Observatory (OCO-2)
46 (Crisp et al., 2004), and Chinese Carbon Satellite (TanSat) (Liu et al., 2013), have greatly improved our understanding of the
47 variation in atmospheric CO₂ concentration and carbon sources and sinks at a global and regional scale. There have been
48 several full-physics retrieval algorithms specially developed for retrieving XCO₂ from the GOSAT observed spectrum,
49 mainly including the NASA Atmospheric CO₂ Observations from Space (ACOS) (O'Dell et al., 2012), the National Institute
50 for Environmental Studies (NIES) (Yoshida et al., 2013), the University of Leicester full-physics XCO₂ (OCFP) (Cogan et
51 al., 2012) and the RemoTeC XCO₂ Full Physics (SRFP) (Butz et al., 2011).

52 Retrieval of XCO₂ from space is susceptible to the effects of light path changes due to aerosol scattering, uncertainties
53 in observed spectrum and surface states (O'Dell et al., 2012; Oshchepkov et al., 2013). The bias and performance of XCO₂
54 retrievals from an algorithm could change in different regions with differing land surfaces and anthropogenic emissions.
55 Spatio-pattern attributions of XCO₂ viewed from different algorithms are also different, even in the same region, due to
56 different physical approaches adopted by the algorithms, assumptions of atmospheric conditions (aerosol, surface pressure,
57 CO₂ profile, etc.), and pre- and post-processing filters. Currently, the validation of XCO₂ retrievals from different algorithms
58 focuses on using ground-based measurements from Total Carbon Column Observing Network (TCCON) sites (Wunch et al.,
59 2011; Yoshida et al., 2013; Hewson, 2016; Buchwitz et al., 2015, Detmers et al., 2015, Oshchepkov et al., 2013) and their
60 consistency evaluation and cross-comparison both at a global scale and in continental regions (Kulawik et al., 2016;
61 Lindqvist et al., 2015; Lei et al., 2014). The precision and uncertainty of satellite-retrieved XCO₂ outside TCCON stations,
62 most of which are located remote from regions with abundant biosphere fluxes and human activities, are still not well
63 evaluated. The sparseness of TCCON stations over the globe, moreover, means a lack of enough ground observations to
64 validate satellite retrievals. Specifically, there are no good TCCON data available in China, and only a few satellite retrievals
65 have been validated using ground-based Fourier Transform Spectrometer (FTS) XCO₂ measurements in Hefei (Wang et al.,
66 2017). In the analysis and application of XCO₂ data from ACOS, NIES, OCFP and SRFP, we found that unreasonably high

67 XCO₂ was presented in the Taklimakan desert in China (Bie et al., 2016; Liu et al., 2015). For this reason, we extended the
68 study scope to select a longer study period and to further assess the overall performance of these four algorithms at a
69 regional scale.

70 With the advantage of continuity in space and time, atmospheric transport model simulation of CO₂ has been widely
71 used in assessing the performance of satellite-retrieved XCO₂ (Cogan et al., 2012; Lindqvist et al., 2015; Kulawik et al.,
72 2016). As anthropogenic emission of CO₂ is the major contributor to increases of CO₂ in the atmosphere, many studies have
73 been involved in deriving estimates of anthropogenic CO₂ emissions (Oda et al., 2011; Andres et al., 2011). It is known that
74 there exists high uncertainty in estimates of CO₂ emissions from both the burning of fossil fuel and cement production (FF
75 CO₂ emissions) throughout China (Guan et al., 2012; Liu et al., 2015). As noted by Andrews et al. (2012), there exist many
76 kinds of restrictions (e.g., commercial competitiveness reasons) in obtaining accurate data on sub-national (e.g., large-point-
77 source or provincial) FF CO₂ emissions. Furthermore, the assumption of uniform per-capita emissions within a country has
78 also been shown to be unreliable for large countries with diversified economies and electricity-generation methods (Nassar et
79 al., 2013). In the previous study of Keppel-Aleks (2013), the simulated Chinese XCO₂ data was increased by a national
80 uniform ratio for the corresponding XCO₂ contributed by fossil sources to account for the underestimation in Chinese
81 emissions, in which way the spatial variability of Chinese FF emissions was not considered sufficient.

82 In this paper, we focus on a latitude band of 37°N-42°N from 80°E to 120°E in China, where there are various typical
83 land covers such as desert, including the Taklimakan desert, and grassland and built-up areas mixed with croplands,
84 including the megacity of Beijing, and there are anthropogenic emissions increasing ~~that trend from small amounts to large~~
85 ~~amounts~~ from west to east. In this band, the inconsistencies of XCO₂ values derived from four algorithms including ACOS
86 V3.5, NIES V02.21, OCFP V6.0 and SRFP V2.3.7 are compared and evaluated in this paper. A forward model simulation
87 data set from GEOS-Chem, moreover, is also used for intercomparison. To improve the simulation of CO₂ concentration by
88 GEOS-Chem, we introduced a new emission data set, the Chinese High Resolution Emission Gridded Data (CHRED) which
89 is produced by the Ministry of Environmental Protection, China (MEP) based on investigations of emitting point sources
90 from approximately 150 million enterprises throughout the country in 2012 (Wang et al., 2014; Cai et al., 2014).

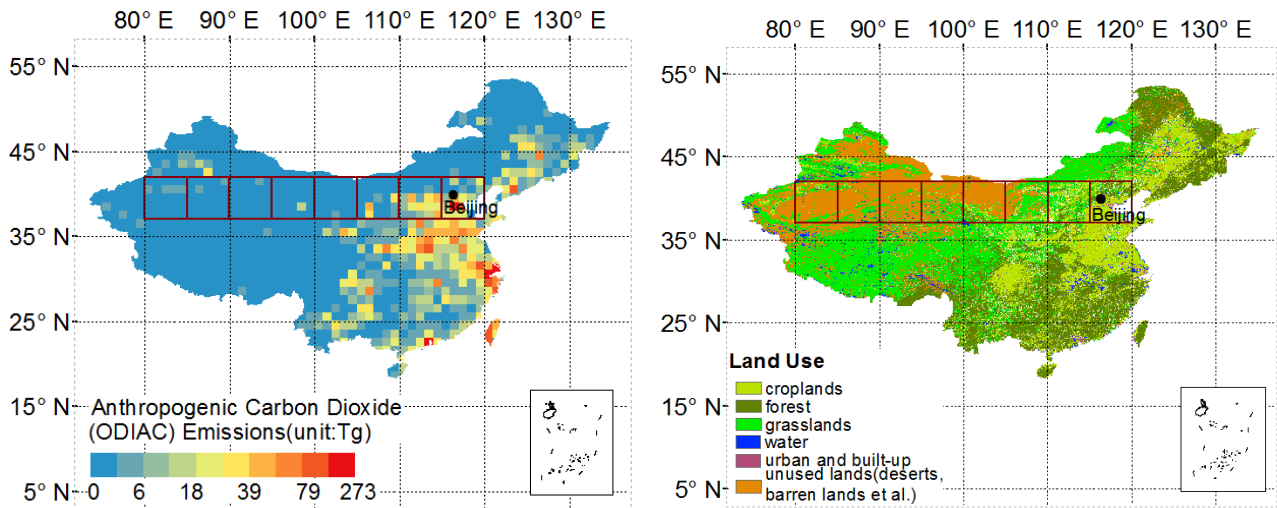
91 First, we aim to reveal the regional uncertainty of XCO₂ observed by GOSAT for the different land covers and
92 anthropogenic CO₂ emission regions by quantifying the inconsistency of the four retrieval algorithms. Second, we aim to
93 provide a reasonable and valuable reference for the analysis and application of XCO₂ data when using these XCO₂ data from
94 the four algorithms. Sec. 2 in this paper describes the XCO₂ retrievals data from four algorithms and the implementation of
95 XCO₂ simulated by GEOS-Chem using CHRED. Inconsistencies of XCO₂ datasets among the four algorithms are quantified
96 and evaluated by (1) pairwise comparisons of XCO₂ between algorithms and (2) comparisons with GEOS-Chem simulations
97 in Sec. 3. The spatio-temporal patterns of XCO₂ from each algorithm are investigated using a combination of sine and cosine
98 trigonometric functions to fit monthly averaged XCO₂ from March 2010 to February 2013 in Sec. 4. Furthermore, the most
99 likely attribution-affecting factors on regional inconsistency, including aerosol and surface albedo, are discussed in Sec. 5.
100 The latest ACOS V7.3 dataset, moreover, is also ~~evaluated~~ used by cross-comparisons with GEOS-Chem and other

101 algorithms including ACOS V3.5, NIESV02.21, OCFP V6.0 and SRFP V2.3.7, as shown in subsections of Sec. 5. Finally,
102 the regional performances of four algorithms and the regional uncertainty of GOSAT XCO₂ retrievals from the results
103 described above are summarized, and conclusions are given in Sec. 6.

104 **2 Study area and data**

105 **2.1 Study area**

106 The latitude band of 37°N~42°N from 80°E to 120°E in China is selected as the study area, which is segmented into eight
107 cells in a grid of 5°x5° units for comparison and evaluation. The study area has two typical surface characteristics as shown
108 in Fig. 1, supporting our assessment of the performance of XCO₂ retrievals from four algorithms: (1) the amounts of
109 anthropogenic CO₂ emissions from west to east significantly varies from small to large as shown in Fig. 1(a). The emission
110 data are from the Open-source Data Inventory for Anthropogenic CO₂ (ODIAC), a global annual fossil fuel CO₂ emission
111 inventory developed by combining a worldwide point-source database and satellite observations of the global nighttime
112 distribution (Oda et al., 2011). There are almost no anthropogenic CO₂ emissions in the western cells ending at 105°E, while
113 there is high anthropogenic emission located in the cells on the eastern end of the latitude band. (2) There are typical land
114 covers from west to east, as shown in Fig. 1 (b), mainly composed of desert (desert sand in the two cells from 80°E to 90°E,
115 Gobi in the two cells from 90°E to 100°E, desert sand in the cell of 100°E-105°E), grassland in the cell of 105°E-110°E, and
116 cropland and built-up areas in the two cells from 110°E to 120°E. These characteristics are associated with complicated
117 aerosol compositions and loadings. One of the main reasons for focusing on this latitude band, moreover, is because there are
118 more high-quality GOSAT scans available in this area compared to other areas in China.



119

120 **Fig. 1. (a) Location of the study area segmented into cells (deep red cells) in China and annual fossil fuel CO₂ emission in 2012 (1 x**
 121 **1 degree) from ODIAC and (b) land use mapping in 2010, where the black dot represents Beijing, the capital of China.**

122

123 2.2 GOSAT XCO₂ dataset derived from four algorithms

124 We collected XCO₂ data from March 2010 to February 2013 derived from four algorithms: ACOS V3.5
 125 (<http://CO2.jpl.nasa.gov>), NIES V02.21 (RA version with GU screening scheme) (<https://data2.gosat.nies.go.jp>), OCFP
 126 V6.0 (<http://www.esa-ghg-cci.org>) and SRFP V2.3.7 (<http://www.esa-ghg-cci.org>). AOD and surface albedo in 0.75-um O₂
 127 band, which are necessary for our further analysis, are also collected from attached datasets in each algorithms except that
 128 albedo is not available for OCFP. The major characteristics of the four algorithms and the relevant references are listed in
 129 Table 1. The validation at TCCON sites for all algorithms indicates that the bias is less than 1.2 ppm on average and that the
 130 standard deviation is less than 2.0 ppm. All algorithms take aerosol optical depth (AOD) into consideration in their data
 131 screening scheme but in slightly different ways. ~~The recommended bias corrections are applied to the collected XCO₂ data~~
 132 ~~from ACOS, OCFP and SRFP.~~ The collected XCO₂ data from ACOS, OCFP and SRFP are the products after bias
 133 correction. Data observed with high gain and passing the corresponding recommended quality control criteria are used in
 134 ACOS, NIES, OCFP and SRFP.

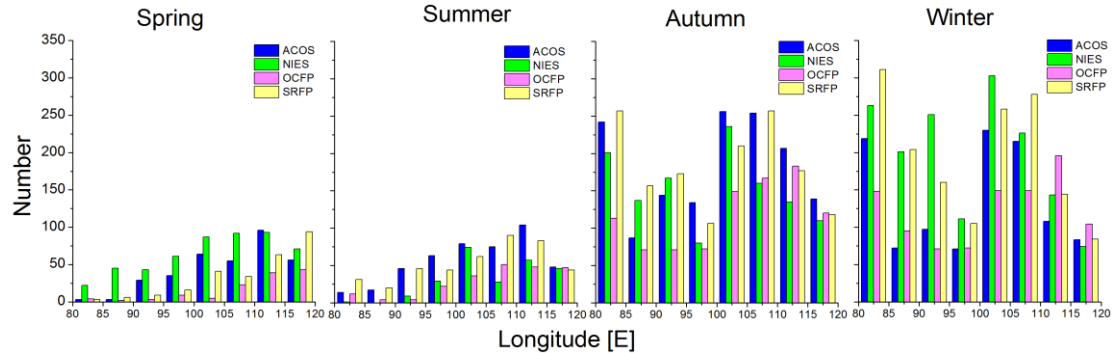
136 **Table 1 Summary of validating results with TCCON, data screening schemes, consideration in scattering and bias corrections for**
 137 **the four retrieval algorithms.**

	ACOS	NIES	OCFP	SRFP
Validation with TCCON ^{*1}	0.3 ppm 1.7 ppm	-1.2 ppm 2.0 ppm	0.04 ppm 1.78 ppm	0.01 ppm 1.93 ppm
Data screening schemes	Aerosol_total_aod: 0.015 to 0.25 Sounding_altitude:<3000 0.55<XCO ₂ _uncer<2.0 ppm Aod_dust<0.15 The difference of the retrieved and priori surface pressure from the A-band cloud-screen $\Delta P_{s,cl d}$: (-12,4.1) hPa	Retrieved aerosol optical thickness: <=0.1 Difference of retrieved and a priori surface pressure: <=20 hpa Blended albedo: <1	Retrieved type 1 (small) AOD: <=0.3 Retrieved type 2 (large) AOD: <=0.15 Retrieved ice type AOD: <=0.025 Error on retrieved XCO ₂ :<=2.15	Aerosol optical thickness : <0.3 3<aero_size<5 0<aerosol_filter<300 Error on retrieved XCO ₂ : <1.2 ppm standard deviation of surface elevation within GOSAT ground pixel: <80 m Blended albedo: <0.9
Consideration in scattering	4 extinction profiles (two aerosol types , water and ice cloud)	logarithms of the mass mixing ratios of fine-mode aerosols and coarse mode aerosols with aerosol optical properties based on SPRINTARS V3.84	Aerosol profile scaling of 2 different aerosol types; cloud extinction profile scaling	Aerosol particle number concentration, aerosol size parameter, aerosol height
Bias corrections	$X'_{CO_2} = X_{CO_2} - 0.5 - 0.155 * (\Delta P_{s,cl d} + 2.7) + 10.6 * (\alpha'_3 - 0.204) + 0.0146 * (\Delta GRAD_{CO_2} - 35) + 12.8 * (AOD_{DUST} - 0.01)$ See details in the product user guide.	-	Via a regression analysis of the difference between GOSAT and TCCON XCO ₂ land observations. See details in the product user guide	$X'_{CO_2} = X_{CO_2} * (1.002837 + 2.1176e - 5 * \phi)$ ϕ : the aerosol filter
References	GES DISC, 2016; O'Dell et al., 2012; D.Wunch et al., 2011.	NIES (GOSAT Project Office), 2015; Yoshida et al., 2013; D.Wunch et al., 2011.	Hew, 2016; GHG-CCI group at University of Leicester, 2014.	Detmers et al., 2015; Hasekamp et al., 2015

138 ^{*1}The first represents mean biases, and the second represents overall standard deviations.

139 Within the study area, the total numbers of valid GOSAT XCO₂ observations are 3345, 3556, 2282 and 3685 for ACOS,
 140 NIES, OCFP and SRFP, respectively. Figure 2 shows the number of available XCO₂ retrievals for 4 seasons (spring: MAM;
 141 summer: JJA; autumn: SON; winter: DJF). It can be seen that the number of available XCO₂ retrievals is clearly smaller in
 142 spring and summer than that in autumn and winter due to different meteorological conditions and data-screening processes.

143 The cloudiness in spring and summer caused by the monsoon climate disturbs satellite observation, while the smaller data
144 number in the west of 110 °E is due to frequent dust storm in the Taklimakan Desert.



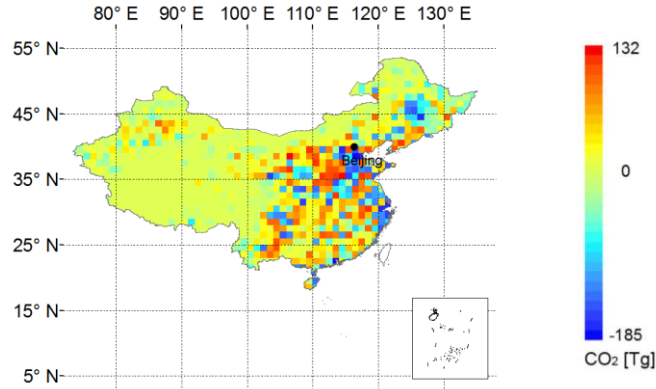
145

146 **Fig. 2. Number of single scans from the four GOSAT-XCO₂ data sets from ACOS, NIES, OCFP and SRFP over each 5x5 ° cells for**
147 **different seasons (Spring: MAM; summer: JJA; autumn: SON; winter: DJF) from March 2010 to February 2013.**

148 2.3 XCO₂ simulations from GEOS-Chem

149 We use GEOS-Chem version 10-01 driven by GEOS-5 and the details of the main input emissions are as follows: 1) Fossil
150 fuel fluxes are taken from the new emission data set CHRED for the Chinese mainland, we also use ODIAC version 2013 for
151 comparison with CHRED. 2) The balanced biosphere CO₂ uptake and emission fluxes are taken from the Simple Biosphere
152 Model version 3 (SiB3) [Messerschmidt et al. 2012]. 3) Biomass emissions are taken from Global Fire Emission Database
153 version 4 (GFEDv4) (Giglio et al., 2013). 4) Ocean fluxes are taken as Takahashi et al. (2009) suggested. A detailed
154 description of these input emissions for the GEOS-Chem CO₂ simulation is presented in Nassar et al. (2010), although we
155 have used some of the most recent updates available in the GEOS-Chem version 10-01 and the Harvard–NASA Emission
156 Component version 1.0 (HEMCO) module (Keller et al., 2014), a versatile component for emissions in atmospheric models.
157 Higher model resolution is critical in the calculation of the concentrations of atmospheric gases, especially over land where
158 topography smoothing (compared to reality) is determined by horizontal resolution (Ciais et al., 2010). Considering this,
159 GEOS-Chem nested grid model in China at 0.5 ° (latitude) x 0.666 ° (longitude) horizontal resolution, is used for the CO₂
160 simulation with boundary conditions provided by the global model at 2 ° (latitude) x 2.5 ° (longitude) resolution. We made a
161 restart file with 386.4 ppm for both the global simulation and the nested simulation on 1 January 2009 based on NOAA
162 ESRL data. Both the global model and the nested-grid model were run twice, driven by the same CO₂ fluxes from January
163 2009 to February 2013 except that the ODIAC was chosen for the first run and CHRED for the second as the input
164 fossil-fuel fluxes over the Chinese mainland. Model CO₂ profiles (averages for local hours between 12:00 pm and 13:30 pm)
165 were presented from January 2010 to February 2013, allowing sufficient time for the high-resolution model to adjust to
166 transients introduced by the initialization of the model on 1 January 2009. The pressure-weighting function described in
167 Connor (2008) was applied to convert level-based modeling CO₂ to XCO₂.

168 Fig.3 presents the spatial difference of emissions over the Chinese mainland between CHRED and ODIAC at a
169 horizontal resolution of $1^\circ \times 1^\circ$. The values of emissions from CHRED are mostly larger than those from ODIAC, as shown in
170 Fig. 3, and this difference tends to be large in the eastern part of our study area. In addition, the difference in their total
171 emissions, 10.38 Pg CO_2 for CHRED versus 9.64 Pg CO_2 for ODIAC, is not small. ODIAC is also found to exhibit an
172 overestimation of emissions in large cities compared to CHRED.

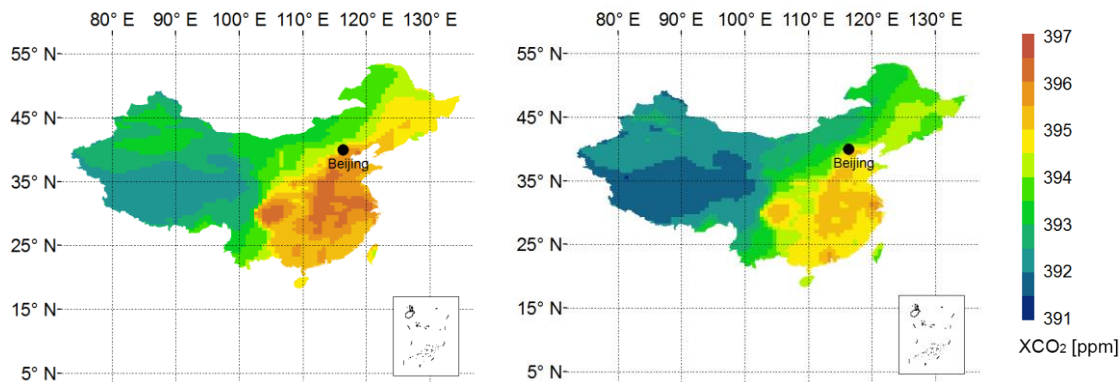


173
174 **Fig. 3. Difference of annual total anthropogenic CO₂ emissions between CHRED and ODIAC in 2012 in China, where the black**
175 **dot represents Beijing, the capital of China.**

176 For each $1^\circ \times 1^\circ$ grid, the corresponding annual CO₂ emissions in the years from 2009 to 2012 were allocated by the ratio
177 of emissions in CHRED to that in ODIAC in 2012. We acquired the new input inventory of CO₂ emissions, CHRED, by
178 scaling the obtained yearly emissions with the ratio of monthly emissions to the yearly ones in ODIAC. In this way, we
179 altered the spatial and temporal distribution, but not at temporal scales finer than monthly. This is expected to be an
180 improvement upon the current ODIAC emission values.

181 The annually averaged XCO₂ simulations, driven separately by CHRED and ODIAC respectively, are calculated and
182 shown in Fig. 4. The impact of emission deviations of CHRED from ODIAC is significant, with XCO₂ from CHRED larger
183 by 0.7 ppm on average over China. There are also obvious differences in spatial patterns, especially in Northwest China,
184 Northeast China, North China and South China. XCO₂ simulations from CHRED are larger by more than 0.7 ppm in most
185 parts east of 100° E with a maximum of 1.4 ppm compared to those from ODIAC. The increase in the annual mean, which
186 should not be ignored, is approximately 1.0 ppm for east of 110° E in the study latitude band. The CO₂ profile dataset from
187 CHRED are used to compare with satellite-retrieved XCO₂ in our following experiments.

188



189

190 **Fig. 4. Annual mean of XCO₂ simulations driven by CHRED (left) and ODIAC (right) in 2012 in China, where the black dot**
 191 **represents Beijing, the capital of China.**

192 We compared GEOS-Chem CO₂ simulations from the global model driven by CHRED with daily mean TCCON data
 193 from 14 TCCON sites (version GGG2014 data version) (Blumenstock et al., 2014; Deutscher et al., 2014; Griffith et al.,
 194 2014a, 2014b; Hase et al., 2014; Kawakami et al., 2014; Kivi et al., 2014; Morino et al., 2014; Sherlock et al., 2014;
 195 Sussmann et al., 2014; Warneke et al., 2014; Wennberg et al., 2014a, 2014b, 2014c). All TCCON measurements between 12
 196 pm and 13:30 pm are used in the comparisons, where GEOS-Chem CO₂ profiles are taken according to the location of
 197 TCCON stations (latitude and longitude) as well as the observing date and transformed to XCO₂ by convolved with the
 198 individual averaging kernel in each station as Wunch (2010) suggested. The statistics results are shown in Table 2.

199 **Table 2. Statistics of comparison between GEOS-Chem CO₂ simulations driven by CHRED and TCCON data from January 2010**
 200 **to February 2013, which includes biases (Δ), the standard deviations (δ), the correlation coefficients (r) and valid days (days) when**
 201 **TCCON data are available. Δ , δ and r are calculated using coincident daily mean data averaged between 12:00 pm and 13:30 pm.**

<u>ID</u>	<u>Station name</u>	<u>Latitude</u>	<u>Longitude</u>	<u>Δ[ppm]</u>	<u>δ[ppm]</u>	<u>r</u>	<u>days</u>
<u>1</u>	<u>Sodankyla</u>	<u>67.37</u>	<u>26.63</u>	<u>2.03</u>	<u>2.00</u>	<u>0.83</u>	<u>269</u>
<u>2</u>	<u>Bialystok</u>	<u>53.23</u>	<u>23.02</u>	<u>0.49</u>	<u>1.84</u>	<u>0.87</u>	<u>196</u>
<u>3</u>	<u>Karlsruhe</u>	<u>49.1</u>	<u>8.44</u>	<u>0.84</u>	<u>1.69</u>	<u>0.84</u>	<u>152</u>
<u>4</u>	<u>Orleans</u>	<u>47.97</u>	<u>2.11</u>	<u>0.44</u>	<u>1.70</u>	<u>0.85</u>	<u>223</u>
<u>5</u>	<u>Garmisch</u>	<u>47.48</u>	<u>11.06</u>	<u>0.65</u>	<u>1.64</u>	<u>0.83</u>	<u>293</u>
<u>6</u>	<u>Park Falls</u>	<u>45.94</u>	<u>-90.27</u>	<u>1.17</u>	<u>2.14</u>	<u>0.75</u>	<u>494</u>
<u>7</u>	<u>Lamont</u>	<u>36.6</u>	<u>-97.49</u>	<u>-0.04</u>	<u>1.22</u>	<u>0.90</u>	<u>642</u>
<u>8</u>	<u>Tsukuba</u>	<u>36.05</u>	<u>140.12</u>	<u>1.43</u>	<u>1.66</u>	<u>0.75</u>	<u>217</u>
<u>9</u>	<u>JPL</u>	<u>34.2</u>	<u>-118.18</u>	<u>-1.30</u>	<u>1.15</u>	<u>0.90</u>	<u>289</u>
<u>10</u>	<u>Saga</u>	<u>33.24</u>	<u>130.29</u>	<u>-0.39</u>	<u>1.65</u>	<u>0.86</u>	<u>159</u>
<u>11</u>	<u>Izana</u>	<u>28.3</u>	<u>-16.48</u>	<u>0.85</u>	<u>1.04</u>	<u>0.90</u>	<u>114</u>
<u>12</u>	<u>Darwin</u>	<u>-12.43</u>	<u>130.89</u>	<u>0.65</u>	<u>0.90</u>	<u>0.88</u>	<u>447</u>
<u>13</u>	<u>Wollongong</u>	<u>-34.41</u>	<u>150.88</u>	<u>0.53</u>	<u>0.83</u>	<u>0.94</u>	<u>347</u>
<u>14</u>	<u>Lauder</u>	<u>-45.04</u>	<u>169.68</u>	<u>0.92</u>	<u>0.42</u>	<u>0.97</u>	<u>370</u>
	<u>Mean</u>			<u>0.59 ± 0.80</u>	<u>1.42 ± 0.50</u>		

202 The results of Table 2 show that the bias ranges from -1.30 to 2.03 ppm for all TCCON sites with standard deviations of
203 the difference varying from 0.42 to 2.14 ppm. The mean standard deviation at the TCCON sites, a measure of the achieved
204 overall precision, from using GEOS-Chem simulations driven by CHRED is 1.42 ± 0.50 ppm which is slightly different
205 from using GEOS-Chem simulations driven by ODIAC (1.41 ± 0.49 ppm). Those validated results with TCCON comparing
206 GEOS-Chem CO₂ simulations driven by CHRED to that by ODIAC indicate that the GEOS-Chem CO₂ simulations driven
207 by CHRED is more likely not to change the global magnitude of CO₂ concentration but rather to depict fine spatial
208 distribution of CO₂ concentration in China.
209

210 **2.4 Aerosol optical depth and surface albedo data**

211 The monthly mean aerosol optical depth (AOD) data were collected from the NASA Earth Observing System's Multi-angle
212 Imaging Spectro-radiometer (MISR) Level 3 Component Global Aerosol Product, downloaded from the website
213 <https://eosweb.larc.nasa.gov/project/misr>. The released GLASS (Glass Land Surface Satellites) albedo product
214 GLASS02B06 (<http://glcf.umd.edu/data/abd/>) is used, which is a gapless, long-term continuous and self-consistent data-set
215 with accuracy similar to that of the Moderate Resolution Imaging Spectrometer (MODIS) MCD43 product (Liu et al., 2013).
216 GLASS02B06 is a daily land-surface shortwave (300-3000nm) broadband albedo product in temporal resolution of eight
217 days.

218 **3 Quantification of agreement of XCO₂ retrievals from four algorithms in the footprints**

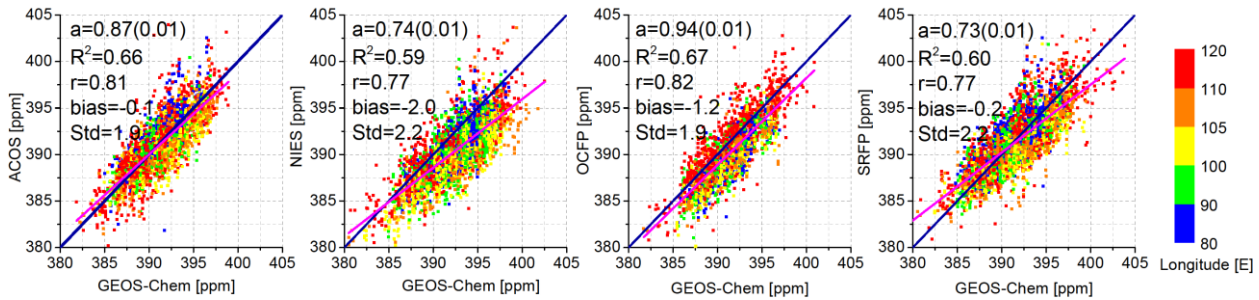
219 We focus on the difference of each footprint XCO₂ retrieval in this section. Comparison of XCO₂ from four algorithms with
220 GEOS-Chem CO₂ simulations driven by CHRED, and pairwise comparisons of XCO₂ between algorithms were calculated
221 as a quantified indicator of their differences.

222 **3.1 Comparisons with GEOS-Chem CO₂ simulations**

223 We used the nested GEOS-Chem CO₂ simulations driven by CHRED as a baseline to quantify the regional consistency of
224 the four algorithms. The collocated model CO₂ profile is averaged over the local hours of 12:00-13:30 pm corresponding to
225 the local time of overpass and locations (latitude and longitude) of GOSAT. To compare XCO₂ retrievals from ACOS, NIES,
226 OCFP and SRFP, corresponding GEOS-XCO₂ data were created by applying averaging kernels from each algorithm to
227 model CO₂ profiles as suggested by Rodgers (2003). Correlation diagrams of XCO₂ between GEOS-Chem (X) and GOSAT
228 (Y) for the four algorithms are shown in Fig. 5. The regression slope (a), the coefficient of determination (R²), the correlation
229 coefficient (r), and biases of GOSAT (Y) from GEOS-Chem(X) are also shown in the inset of each panel.

230 It can be seen from Fig. 5 that the linear fits and the correlations with GEOS-Chem are better for ACOS and OCFP (R²
231 approximately 0.66) than for either NIES or SRFP (R² approximately 0.59). The regression slope is the closest to unity in the

232 OCFP panel (0.94) and is lightly less than OCFP in the ACOS panel (0.87), which means the best similarity in variation. The
 233 slope is less than 0.8 in the NIES and SRFP panels. The bias of GEOS-Chem vs ACOS and SRFP is less than 0.5 ppm while
 234 it is 2 ppm and 1.2 ppm vs NIES and OCFP, respectively.



235

236 **Fig. 5: Correlation diagrams of GOSAT XCO₂ (Y) for the four algorithms vs GEOS-XCO₂ (X). Statistics from linear regression fit**
 237 **are also shown. GEOS-Chem data are selected according to the locations and time of XCO₂ retrievals from the four algorithms in**
 238 **cells. Deep blue solid lines represent 1:1 lines, and the magenta lines demonstrate the best linear regression fit for all samples.**
 239 **Colored points represent XCO₂ for different longitude cells in the study latitude band [37°N, 42°N] shown in Fig.1, where colors**
 240 **for each cell are indicated in the right legend.**

241 Table 3 shows the biases and number of samples used between each algorithm and GEOS-Chem in each cell. It can be
 242 seen that the biases of ACOS and SRFP vs GEOS-Chem in all cells are below 1 ppm, which implies better consistency with
 243 GEOS-Chem regionally than NIES and OCFP. NIES presents 1.2-3.1 ppm lower than GEOS-Chem in all cells excluding
 244 the cell of 115°E, which is likely due to no corrections of the existing systematic biases in the NIES data set (Yoshida et al.,
 245 2013). The bias of OCFP vs GEOS-Chem is larger than 1.2 ppm toward the west of 110°E, while it is 0.1 ppm toward the
 246 east of 110°E. The standard deviations of all the four algorithms with GEOS-Chem range from 1.4 ppm to 2.5 ppm in all
 247 cells.

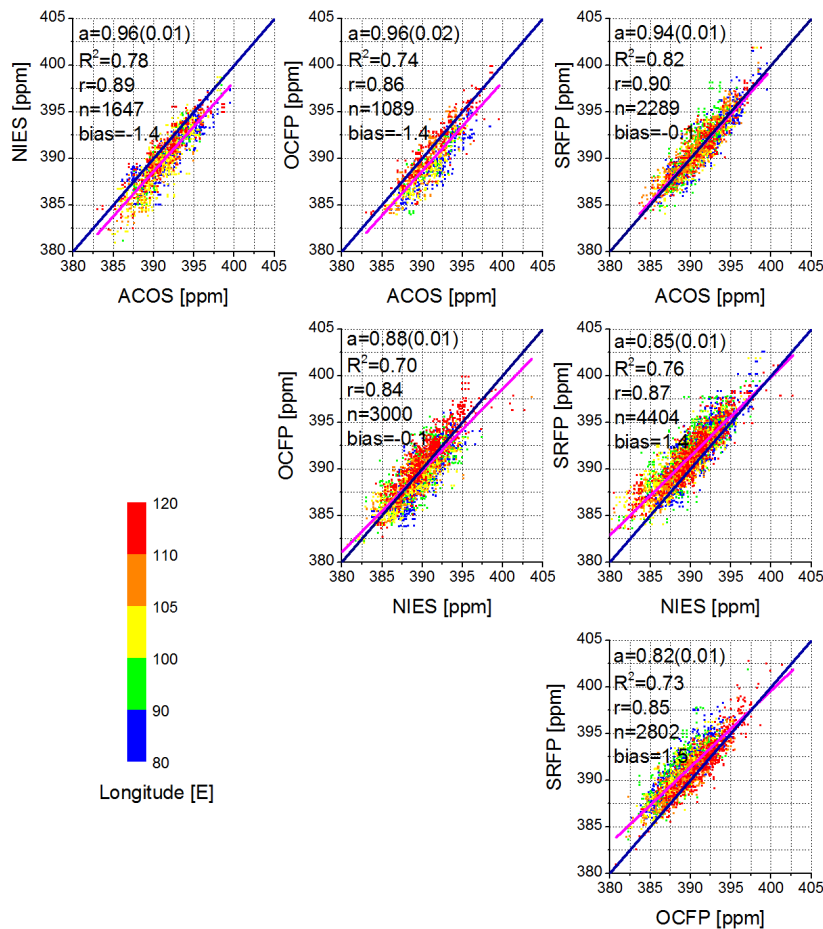
248 **Table 3. The biases (ppm) and their standard deviations (ppm) of the four algorithms vs GEOS-Chem in each cell, where the**
 249 **upper line indicates bias (the corresponding standard deviations in parenthesis) for each algorithm vs GEOS-Chem and the lower**
 250 **line is the available number of used samples. The biases, larger than 1 ppm, are highlighted in bold and underlined.**

Left longitude of cells(°E)	80	85	90	95	100	105	110	115
ACOS	0.7(1.6) 478	0.5(1.6) 179	-0.4(1.4) 316	-0.3(1.5) 303	-0.7(1.7) 629	-0.7(1.7) 599	0.0(2.2) 515	0.5(2.1) 326
NIES	<u>-1.4</u> (1.7) 487	<u>-1.6</u> (1.8) 383	<u>-1.6</u> (1.8) 470	<u>-2.3</u> (2.5) 281	<u>-3.0</u> (1.9) 700	<u>-3.1</u> (2.2) 506	<u>-1.6</u> (2.5) 428	-0.7(2.4) 301
OCFP	<u>-1.8</u> (1.4) 277	<u>-1.8</u> (1.5) 172	<u>-2.2</u> (1.4) 149	<u>-1.2</u> (2.0) 175	<u>-2.3</u> (1.6) 339	<u>-1.5</u> (1.6) 390	-0.1(1.9) 466	-0.1(2.1) 314
SRFP	0.1(1.9) 602	0.0(1.8) 387	0.2(1.7) 388	-0.2(2.0) 271	<u>-1.2</u> (1.9) 571	-0.6(2.7) 659	0.2(2.4) 467	0.0(2.4) 340
EMMA	<u>0.6</u> (1.8) 400	<u>0.2</u> (2.0) 229	<u>-0.4</u> (1.4) 211	<u>-0.2</u> (1.7) 222	<u>-0.8</u> (1.8) 484	<u>-1.0</u> (2.0) 460	<u>-0.1</u> (2.1) 453	<u>-0.1</u> (2.1) 337

251

252 3.2 Pairwise comparisons of XCO₂ between algorithms

253 We made comparisons of geometrically and timely matching pairs XCO₂ between algorithms in each cell. The pairs of
 254 XCO₂ retrievals were matched between two algorithms timely in the same day and geometrically located within $\pm 0.01^\circ$ in
 255 latitude and longitude. Figure 6 shows pairwise comparisons of XCO₂ retrievals between two algorithms that demonstrate
 256 the regression slope (a), the coefficient of determination (R^2), the correlation coefficient (r), the number of matching pairs (n)
 257 and the biases between every pair of algorithms.
 258



259

260 **Fig. 6: Algorithm correlation diagrams and statistical characteristics (insets of panels).** GOSAT-Y observations were selected over
 261 land within $\pm 0.01^\circ$ latitude/longitude of each GOSAT-X observation and in the same day. Deep blue solid lines represent 1:1 lines,
 262 and the magenta ones display the best linear regression fit for all observations. Colored points represent XCO₂ for different cells:
 263 blue-[80 E, 90 E], green-[90 E, 100 E], yellow-[100 E, 105 E], orange-[105 E, 110 E], and red-[110 E, 120 E] in the study latitude
 264 zone [37 N, 42 N].

265 It can be seen from Fig. 6 that ACOS generally demonstrates the best agreement with other algorithms (top panel).
 266 OCFP generally presents biases larger than 1.4 ppm with other algorithms except for 0.1 ppm compared to NIES. It can also

267 be seen from the colored points in Fig. 6 that matching pairs of XCO₂ for OCFP vs ACOS and SRFP mostly concentrated
 268 along the 1:1 line in the eastern cells of 105-120 °E (orange and red points) but drifted from the 1:1 line in the western cells
 269 of 80-100 °E (blue and green points).

270 The differences(biases) of matching pairs (the number ranging from 11 to 945) of XCO₂ between two algorithms,
 271 moreover, were calculated for each cell as shown in Table 4, and the totally averaged absolute differences of matching pairs
 272 of XCO₂ for an algorithm with the other algorithms were also calculated in each cell as shown in Table 5.

273 It can be found from Table 4 that the difference is mostly less than 1 ppm in those eastern cells with a longitude greater
 274 than 105 °E, and their consistency can be seen in Fig. 6 (red points between 110-120 °E) as well. The differences that are
 275 larger than 2 ppm are located in western cells with longitudes less than 105 °E, and these differences are mostly shown in
 276 OCFP vs other algorithms. The total differences shown in Table 5, moreover, indicate that the differences of the four
 277 algorithms tend to be similar to the results of matching pairs of XCO₂ (Table 4), and NIES presents the largest difference up
 278 to 1.6 ppm in the western cells of 95 °E.

279 **Table 4. Differences (ppm) between two algorithms (column algorithm minus row algorithm) and the corresponding standard**
 280 **deviation (ppm) for each cell, where values in parentheses are the corresponding standard deviations. The differences, larger than**
 281 **1.5 ppm, are highlighted in bold and underlined.**

	*	NIES	OCFP	SRFP	EMMA	*	NIES	OCFP	SRFP	EMMA
ACOS		-1.4(1.2)	<u>-2.6</u> (1.2)	-0.5(1.2)	0.2 (1.0)		<u>-1.6</u> (1.6)	<u>-2.0</u> (1.1)	-0.2(1.2)	0.2 (1.1)
NIES	80		-0.9(1.4)	1.1(1.4)	<u>1.7</u> (1.5)	100		-0.4(1.4)	1.4(1.5)	<u>1.6</u> (1.4)
OCFP	°E			<u>2.0</u> (1.2)	<u>2.6</u> (1.5)	°E			<u>1.7</u> (1.3)	<u>1.9</u> (1.4)
SRFP					0.4 (1.1)					0.3 (1.1)
ACOS		<u>-2.0</u> (1.3)	<u>-1.9</u> (1.2)	-0.1(1.2)	0.5 (0.9)		<u>-1.6</u> (1.3)	-0.6(1.4)	0.2(1.2)	0.2 (0.9)
NIES	85		-0.4(1.6)	1.5(1.3)	<u>2.0</u> (1.5)	105		0.2(1.5)	1.2(1.3)	<u>1.5</u> (1.3)
OCFP	°E			<u>2.3</u> (1.4)	<u>2.7</u> (1.5)	°E			1.0(1.3)	1.0 (1.0)
SRFP					0.2 (1.2)					0.2 (0.9)
ACOS		-1.2(1.1)	<u>-1.7</u> (1.1)	0.8(1.4)	0.5 (0.8)		-1.2(1.3)	-0.9(1.4)	0.0(1.4)	0.4 (1.1)
NIES	90		-0.8(1.4)	<u>2.0</u> (1.4)	1.5 (1.2)	110		0.7(1.3)	1.5(1.6)	<u>1.5</u> (1.3)
OCFP	°E			<u>2.4</u> (1.5)	<u>2.0</u> (1.3)	°E			0.5(1.2)	0.7 (1.0)
SRFP					-0.1 (1.1)					0.0 (1.3)
ACOS		<u>-3.0</u> (1.1)	-0.9(1.7)	-0.3(1.2)	0.0 (1.1)		-0.6(1.3)	0.1(1.0)	-0.1(1.0)	0.5 (1.0)
NIES	95		0.5(2.1)	1.3(2.0)	<u>1.7</u> (1.9)	115		0.8(1.5)	0.9(1.3)	<u>1.3</u> (1.5)
OCFP	°E			<u>1.8</u> (1.6)	1.4 (1.1)	°E			0.2(1.3)	0.5 (1.0)
SRFP					0.2 (1.3)					0.6 (0.9)

282 The columns labeled with * represent the left longitude of cells (°E).

283 **Table 5. The average of the absolute differences (ppm) and standard deviation (ppm) of the target algorithm (in column) matching**
 284 **all other algorithms for each cell. Values in parentheses are the corresponding standard deviations. The differences, which are**
 285 **larger than 1.5 ppm, are highlighted in bold and underlined.**

Left longitude of cells(°E)	80	85	90	95	100	105	110	115
ACOS	<u>1.5</u> (0.8)	1.4 (0.7)	1.2 (0.4)	1.6 (1.0)	1.4 (0.6)	1.1 (0.4)	1.1 (0.2)	0.9 (0.2)

NIES	1.6(0.2)	1.8(0.4)	1.6(0.4)	2.2(0.6)	1.6(0.3)	1.5(0.3)	1.5(0.3)	1.3(0.2)
OCFP	2.2(0.6)	2.1(0.6)	1.9(0.5)	1.7(0.2)	1.7(0.4)	1.2(0.1)	1.1(0.1)	1.0(0.2)
SRFP	1.3(0.5)	1.4(0.7)	1.6(0.8)	1.4(0.6)	1.3(0.5)	1.1(0.3)	1.2(0.4)	1.0(0.2)
EMMA	1.6(0.9)	1.6(1.0)	1.3(0.6)	1.3(0.6)	1.3(0.6)	1.1(0.5)	1.1(0.4)	1.0(0.4)

286

Left longitude of cells(°E)	80	85	90	95	100	105	110	115
ACOS	1.3(1.1)	1.2(1.0)	1.0(0.7)	1.4(1.2)	1.2(0.9)	1.0(0.7)	0.9(0.6)	0.7(0.5)
NIES	1.1(0.7)	1.3(0.9)	1.2(0.9)	1.6(1.2)	1.1(0.8)	1.1(0.8)	1.1(0.8)	0.9(0.6)
OCFP	1.5(1.1)	1.4(1.0)	1.4(1.0)	1.3(0.9)	1.2(0.9)	0.9(0.6)	0.8(0.6)	0.8(0.6)
SRFP	1.1(0.9)	1.2(1.0)	1.4(1.1)	1.2(0.9)	1.1(0.8)	0.9(0.6)	1.0(0.7)	0.8(0.5)

287

288 To summarize the quantification and analysis in this section, XCO₂ retrievals from two algorithms, ACOS and SRFP
289 are mostly consistent, and the bias of ACOS from GEOS-Chem is the least among the four algorithms. The difference of
290 XCO₂ from cross-comparing four algorithms tends to be less in cells east of 100°E than that in the cells west of 100°E.

291 4 Comparison of the spatio-temporal pattern revealed by XCO₂ from the four algorithms and simulation

292 We used a combination of sine and cosine trigonometric functions to statistically fit the seasonal variation of XCO₂, which
293 was originally proposed by Keeling et al. (1976) and has been applied extensively in many studies (Thoning et al. 1989;
294 Kulawik et al., 2016; Lindqvist et al., 2015; Zeng et al., 2016; He et al., 2017). Better attributions are thus obtained for XCO₂
295 variation in the seasonal cycle and in spatial background patterns by filtering the noise and filling gaps in the original XCO₂
296 data.

297 Firstly, the monthly averaged XCO₂ was calculated in each cell using XCO₂ retrievals; then the fit function (Keeling,
298 1976), expressed as the following equation [1], was applied to the monthly averaged XCO₂ from March, 2010 to February,
299 2013 for the four algorithms and GEOS-Chem.

$$300 \quad X(t) = A_1 \sin 2\pi t + A_2 \cos 2\pi t + A_3 \sin 4\pi t + A_4 \cos 4\pi t + A_5 + A_6 t \quad [1]$$

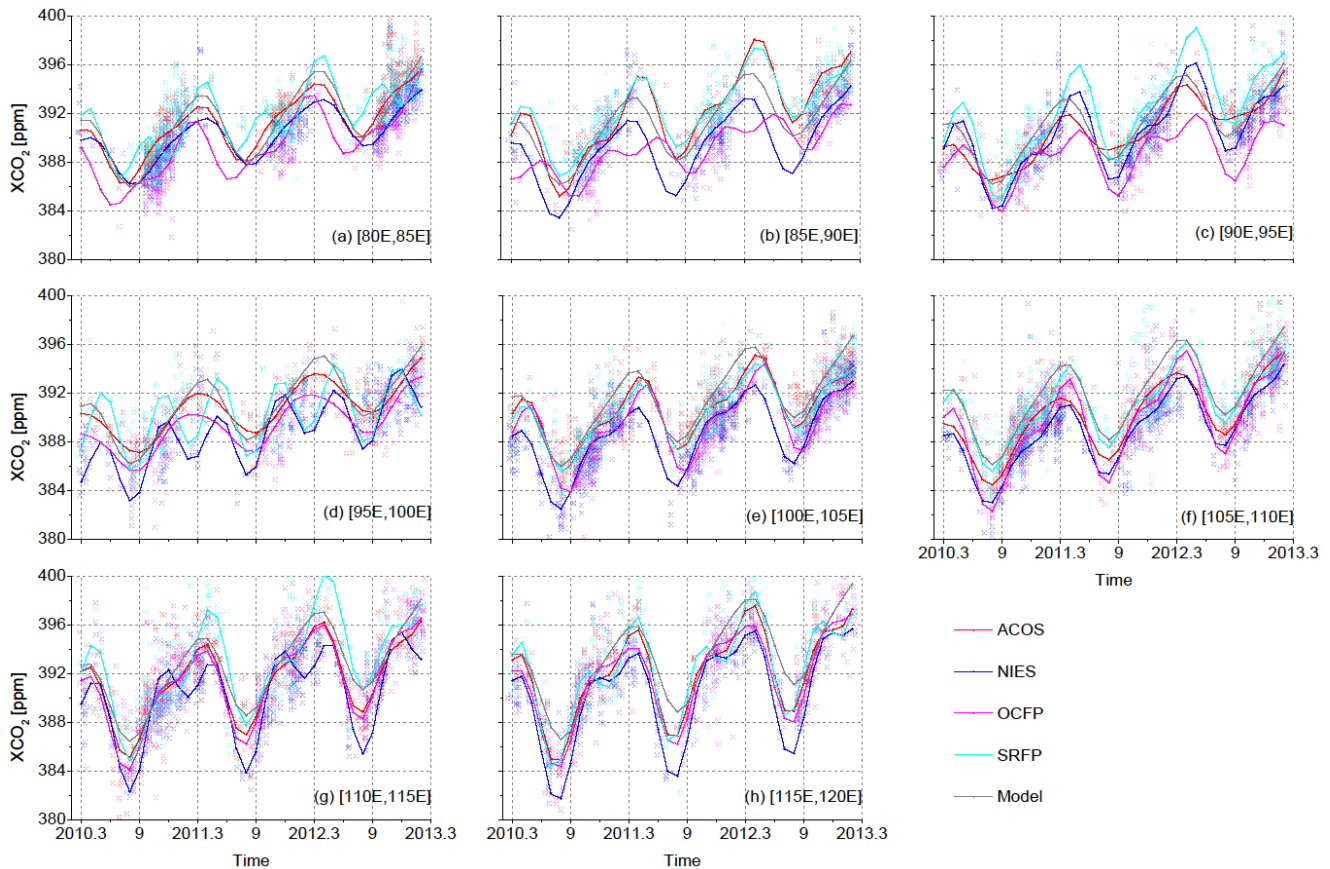
301 where t represents elapsed time in years, A₁-A₄ are the coefficients determining the seasonal cycle, A₅ represents the initial
302 state of XCO₂ with seasonal variation removed, which can be regarded as the corresponding background concentration, and
303 A₆ is the slope of the linear part in the yearly increase ignoring the minor non-linear part. To derive A₁-A₆ with the above
304 formula, least squares were applied to fit the input monthly weighted means with the corresponding standard deviations as
305 measures of errors. The monthly weighted means (e.g., X(t)) and the corresponding standard deviations in each cell were
306 calculated with the weights inversely proportional to the square of retrieval uncertainty in each observation point.

307 The accuracy of fitting X(t) depends on the number of gaps in the available XCO₂ retrievals in time and in space
308 resulting from the filtering mechanism for quality controlling. We introduce the Pearson's correlation, hereafter referred to
309 as R, between the input and the predicted results from equation [1] and the unit weighted mean square error, hereafter

310 referred to as σ , in fitting as an uncertainty to judge whether the fitting results are reasonable or not. In addition, we applied
 311 equation [1] to the GEOS-Chem dataset, which has been converted to XCO_2 as Connor (2008) suggested. Since atmospheric
 312 transport models do not share the same error sources with satellite retrieval algorithms and produces continuous simulations
 313 without data gaps, GEOS-Chem provides helpful a priori information for reference.

314 4.1 Seasonal variation of XCO_2 retrievals

315 The time series in each cell are acquired for each algorithm using the above formula [1]. The monthly fitted XCO_2 from
 316 March 2010 to February 2013 in each cell for the four algorithms as well as GEOS-Chem is shown in Fig. 7. The seasonal
 317 amplitudes (the difference between seasonal cycle maximums and minimums) and uncertainty of the fitting function as
 318 described by R and σ above are demonstrated in Table 6.



319

320 **Fig. 7: The time series from March 2010 to February 2013 in eight cells from the western cell of (a) to the eastern end cell of (h),**
 321 **where colored lines represent the fitting seasonal change trend of the four XCO_2 datasets from the four algorithms, and the**
 322 **colored points represent single XCO_2 retrievals corresponding to four algorithms according to line color: red is for ACOS, blue for**
 323 **NIES, magenta for OCFP and cyan for SRFP. The gray line is the fitting seasonal change trend of XCO_2 simulated by GEOS-**
 324 **Chem.**

325 Table 6: Results of fitted seasonal cycle and the corresponding uncertainty of the fitting results for each cell in the study latitude
 326 band for four algorithms and GEOS-Chem, The symbols “-“ means that filtered results are not available due to large uncertainty
 327 judged by R and σ . R, the correlation coefficient between fitted XCO₂ and monthly averaged original XCO₂ in each cell, less than
 328 0.80, and σ , the unit weighted mean square error in fitting, not less than 3.0, are highlighted in bold and underlined.

Left longitude of cells (°E)	80	85	90	95	100	105	110	115
Seasonal cycle amplitude (ppm)								
ACOS	5.1	7.8	3.7	4.0	6.6	5.9	8.0	9.3
NIES	4.3	6.9	7.8	-	7.1	6.4	9.5	10.7
OCFP	5.3	3.5	-	3.9	7.7	9.2	8.4	8.6
SRFP	6.3	6.5	8.9	-	5.9	7.4	10.4	10.7
GEOS-Chem	6.3	5.9	5.7	5.6	6.5	6.9	7.2	7.9
σ (Unit weight mean square error in fitting)(ppm)								
ACOS	1.2	1.6	1.6	0.6	1.1	1.2	0.4	1.0
NIES	0.7	1.1	1.0	<u>3.0</u>	1.1	1.1	1.5	1.3
OCFP	0.7	0.9	1.5	1.4	1.9	1.1	0.8	0.9
SRFP	1.6	0.7	1.3	<u>3.3</u>	0.8	0.8	1.0	1.0
GEOS-Chem	0.1	0.1	0.1	0.1	0.1	0.1	0.1	0.1
R (Correlations between fitted XCO ₂ and monthly averaged original XCO ₂ in each cell)								
ACOS	0.92	0.92	0.91	0.95	0.91	0.91	0.98	0.94
NIES	0.89	0.91	0.94	<u>0.68</u>	0.96	0.95	0.89	0.92
OCFP	0.90	0.84	<u>0.79</u>	0.84	0.93	0.93	0.93	0.96
SRFP	0.83	0.94	0.92	<u>0.40</u>	0.95	0.94	0.93	0.90
GEOS-Chem	1.00	1.00	0.99	0.99	0.99	0.99	0.99	0.99

329

330 Viewing the attribution of XCO₂ in each cell from Fig. 7 and Table 6, we can find that the seasonal variations from all
 331 XCO₂ retrievals generally show similar changing trends, except for one extra seasonal cycle maximum being misidentified in
 332 some cases mainly due to weaker data constraints for fitting. The timely changing patterns (indicated by seasonal cycle
 333 phases) of all algorithms demonstrate better agreement in the eastern four cells from 100°E to 115°E than those in the
 334 western four cells from 80°E to 95°E. The correlation coefficients of fitting XCO₂ in Table 6 are also significantly greater in
 335 the eastern four cells than those in the western four cells. As a result, the longitude 100°E tends to be a regional border
 336 presenting better consistency of XCO₂ among the four algorithms in its eastern cells than those in its western cells.

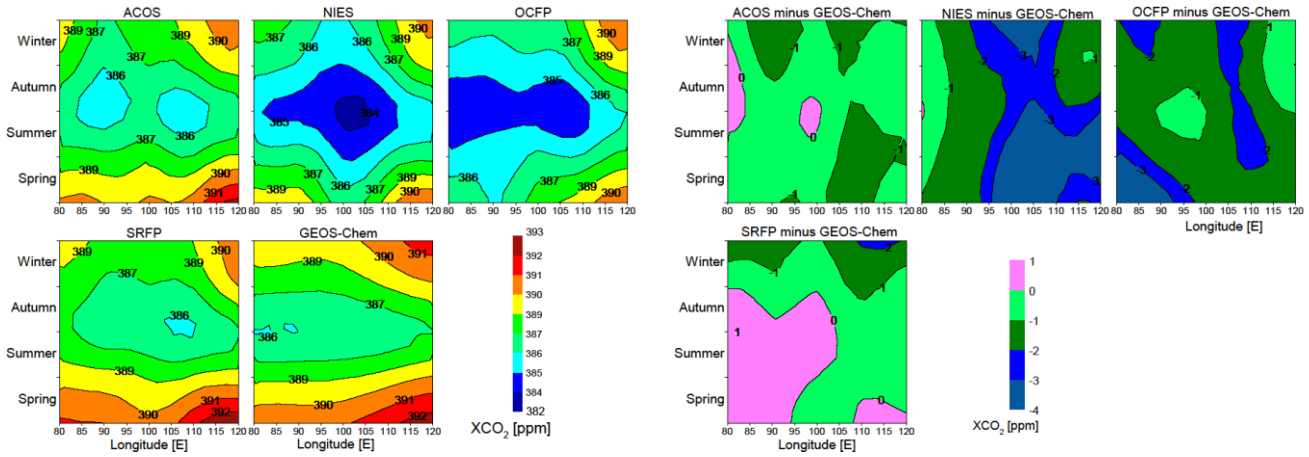
337 Comparing XCO₂ from the four algorithms with GEOS-Chem, one specific result is presented in the eastern-most two
 338 cells from 110°E to 120°E, in which the seasonal amplitudes of XCO₂ are significantly higher from the four algorithms while
 339 the magnitudes of XCO₂ in summer are lower than those from GEOS-Chem as shown in Table 6 and Fig. 7. There is strong

340 CO₂ absorption from farming activities of wheat and corn in the summer (Lei et al., 2010) and anthropogenic CO₂ emission
341 from extra winter heating in these eastern cells. This result is in agreement with an investigation of results over the whole
342 Chinese mainland (Lei et al., 2014) and at 120-180°E over the globe (Lindqvist et al., 2015), which is likely due to the
343 underestimated widespread bio-ecological CO₂ uptake changes that occurred over the past 50 years in atmospheric transport
344 models (Graven et al., 2013).

345 The XCO₂ values from NIES (blue in Fig. 7) are overall lower than those from the other algorithms, which is due to the
346 uncorrected systematic errors -1.2 ppm (refer to Table 1). The seasonal variations from OCFP (magenta in Fig. 7) are
347 abnormal compared to the overall seasonal changing trend of XCO₂ in cells west of 100°E presented for the other three
348 algorithms. The seasonal amplitudes of OCFP presented in Table 6, moreover, are abnormally the lowest in a cell (85-90°E)
349 and the highest in a cell (105-110°E). SRFP and NIES show two abnormal peaks in a cycle of a year in the cell of 95°E,
350 while some large values of σ and small values of R, shown in bold in Table 6, indicate poor fitting mostly in the same cell
351 (95-100°E). These results are likely induced by large gaps in the available XCO₂ data in time series, which leads to a poor
352 fitting constraint.

353 **4.2 Spatio-temporal pattern of detrended XCO₂**

354 We calculated the seasonal averages of the XCO₂ background concentration in each cell after removing the linear yearly
355 increase using the fitting time series of XCO₂ for the four algorithms and GEOS-Chem. The spatio-temporal continuous
356 pattern of background XCO₂ was mapped by Linearly Interpolate Triangulation (Watson et al., 1984) using the seasonal
357 averages of XCO₂ background concentration in each cell for four algorithms and GEOS-Chem, as shown in Fig. 8 (on the
358 left). The spatio-temporal patterns of the differences of detrended XCO₂ to GEOS-Chem simulations for the four algorithms
359 are mapped respectively and are shown in Fig. 8 (on the right).



361

362 **Fig. 8: The spatial (in the study latitude band) and temporal (in seasons) changing patterns of detrended XCO₂ from ACOS, NIES,**
 363 **OCFP, SRFP retrievals and GEOS-Chem simulations (left) and the differences of detrended XCO₂ to GEOS-Chem for between**
 364 **ACOS, EMMA, NIES, OCFP and SRFP and GEOS-Chem.**

365

366 It can be seen from Fig. 8 (on the left) that the spatio-temporal patterns from the three algorithms of ACOS, NIES and
 367 SRFP are generally similar, with an increase spreading outward from the center of each diagram and with the lowest XCO₂
 368 located approximately at 95 °E-105 °E and during the period of summer-autumn; meanwhile, OCFP and GEOS-Chem show a
 369 similar spatio-temporal pattern where the lowest value is not the center. Two common characteristics of XCO₂ spatio-
 370 temporal changes from the four algorithms and GEOS-Chem can also be found: (1) the seasonal changes of XCO₂ are the
 371 same in any of the cells, with lower XCO₂ in summer and autumn than that in spring and winter; and (2) spatial changes of
 372 XCO₂ generally demonstrate larger XCO₂ in the eastern cells than those in the western cells in all seasons. A similarly high
 373 level is captured by ACOS, NIES and SRFP generally in the western deserts with lower CO₂ emissions compared to the
 374 eastern cells with abundant emissions. This feature is especially distinct from ACOS while OCFP and GEOS-Chem both
 show an increasing trend from west to east in any season.

375

376 Comparing the difference to GEOS-Chem (on the right in Fig. 8), the spatio-temporal pattern of ACOS and SRFP
 377 generally demonstrate the smallest values mostly ranging from -1 ppm to 1 ppm. XCO₂ values from both NIES and OCFP
 378 are smaller than GEOS-Chem in space and time, while the XCO₂ difference is mostly 1-3 ppm for NIES and 2 ppm for
 379 OCFP. Regionally, the differences tend to be larger in the western cells than those in the eastern cells for satellite retrievals,
except for OCFP.

380

~~To summarize the quantification and analysis in this section, the spatio-temporal pattern of ACOS tends to be
 381 inconsistent with SRFP. Figure 8 shows two common characteristics among ACOS, NIES, SRFP and EMMA: (1) XCO₂ is
 382 lower in summer and autumn but higher in spring and winter. (2) XCO₂ is higher west of 90 °E and east of 110 °E, while it is
 383 lower in cells 90 °E-110 °E. In addition, XCO₂ values from NIES and OCFP are lower than those from other algorithms,
 384 especially in summer and autumn. A similarly high level is captured by ACOS, EMMA, NIES and SRFP generally in the~~

385 ~~western deserts with lower CO₂ emissions compared to the east, which has abundant emissions. This is distinct from ACOS~~
386 ~~and EMMA, while OCFP and GEOS-Chem both show an increasing trend from west to east in any season.~~

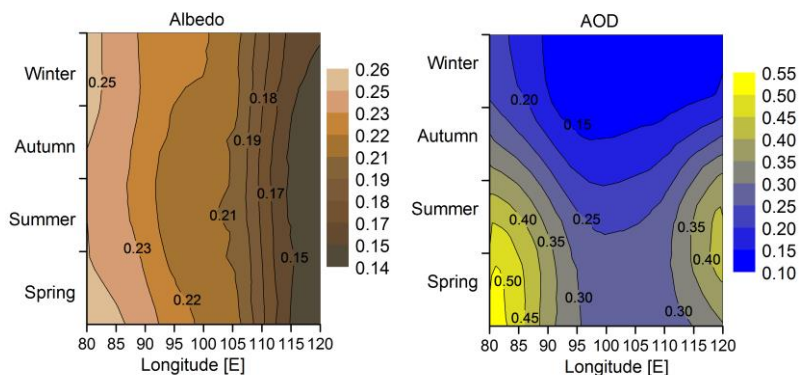
387 5 Discussion

388 In this section, an investigation was made into the most likely attribution of regional inconsistency, i.e., aerosols and albedo,
389 and an additional ~~evaluation-comparison~~ was made ~~of-with~~ the latest released ACOS V7.3, the newer version of ACOS data
390 retrieved by the OCO-2 algorithm, using GEOS-Chem simulations and retrievals from other algorithms including ACOS
391 V3.5, NIESV02.21, OCFP V6.0 and SRFP V2.3.7.

392 5.1 Discussion of albedo and aerosol effects for XCO₂ retrieval

393 The above quantification and analyses indicate that generally good agreements are achieved among the four data sets in the
394 eastern cells, while three out of four GOSAT-XCO₂ data sets present abnormal high concentrations in the western cells. It
395 has been known that aerosols are the most important factor inducing errors in satellite-retrieved XCO₂ (Guerlet et al., 2013;
396 Oshchepkov et al., 2013; Yoshida et al., 2013; O'Dell et al., 2012), while ~~estimations of Aerosol Optical Depth (AOD)~~AOD
397 in GOSAT full physics CO₂ retrieval algorithms are ~~is~~ greatly affected by high surface albedo because of atmospheric
398 multiple scattering of light and the optical lengthening effect~~the optical lengthening effect~~. For that reason, we investigate
399 the spatial and temporal characteristics of aerosols and albedo in our study latitude band to probe the reason why high
400 inconsistency of XCO₂ retrieval algorithms appears in western cells rather than in eastern cells with intensive human
401 activities.

402 The spatial and temporal characteristics of shortwave broadband (300-3000nm) albedo from GLASS albedo products
403 and AOD at 555 nm from MISR aerosol products with seasons in the study area are revealed as shown in Fig. 9, in which
404 they are mapped by the same method as Fig. 8. The seasonal mean AOD and albedo were calculated in spring (MAM),
405 summer (JJA), autumn (SON), and winter (DJF) using the monthly mean AOD and black sky shortwave albedo from
406 January 2010 to December 2012 for every cell.



407

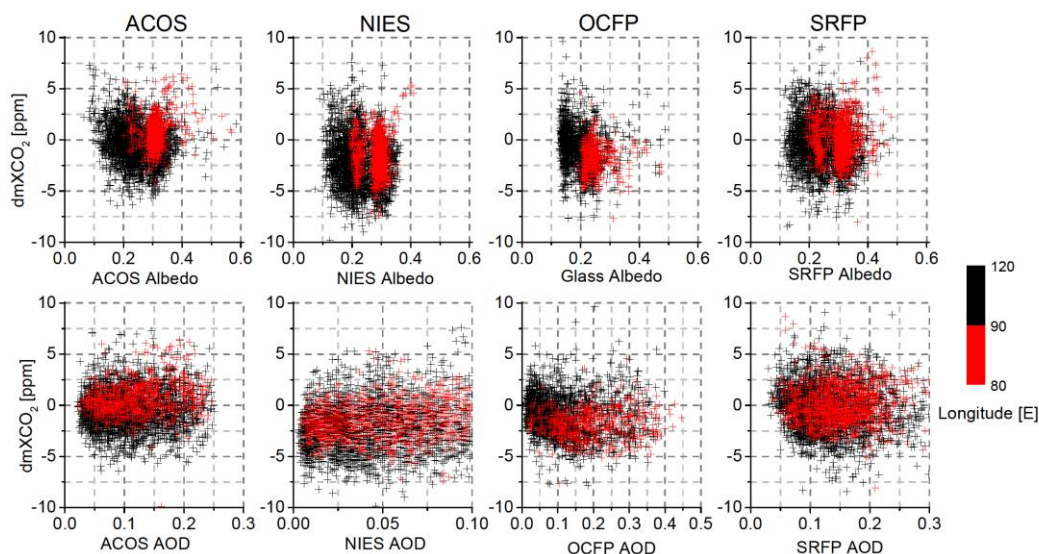
408 | **Fig. 9: The temporal and spatial patterns of black sky shortwave broadband (300-3000nm) albedo (left) and AOD at 555 nm**
 409 **(right). Colors represent albedo (left) and AOD (right).**

410 As shown in Fig. 9, albedo shows small temporal variation with a decreasing trend from west to east. In contrast with
 411 albedo, AOD follows a clear seasonal pattern with a higher level in spring and summer than in autumn and winter. The uplift
 412 of AOD in spring and summer is due to the higher frequency of Asian sand and dust storms for cells west of 105 °E. The
 413 main contributors to aerosol loading east of 110 °E are emissions from urban fugitive dust/fly ash, dust plumes from deserts
 414 in the western and northern China such as the Taklimakan deserts, industrial activities and residential heating (Zhang et al.,
 415 2012). For this reason the inconsistency of XCO₂ from the four algorithms, which tends to be higher in spring and summer
 416 than in autumn and winter in the Taklimakan Deserts in western cells shown in the results above, is likely induced by the
 417 combined effect of high aerosol and high brightness surface (high surface albedo) on retrieval uncertainty.

418 We discussed the influences of albedo and AOD on XCO₂ retrievals from ACOS, NIES, OCFP and SRFP in further.
 419 Fig. 10 plots the scatters of albedo and AOD with the differences between GEOS-XCO₂ data (created in section 3.1) to
 420 XCO₂ retrievals, hereafter referred to as dmXCO₂, for ACOS, NIES, OCFP and SRFP. The albedo data obtained from
 421 GLASS02B06 is used for OCFP as there are no albedo data available from its released data product.

422 Fig. 10 shows that dmXCO₂ of both ACOS and NIES demonstrate a slightly decreasing trend with albedo whereas
 423 slightly increasing trend with AOD. The dmXCO₂ of ACOS tend to be larger in 80 °E -90 °E of deserts with high albedo than
 424 that in other regions. The dmXCO₂ of OCFP demonstrate a clear decreasing trend with albedo and AOD comparing to the
 425 other algorithms. The dmXCO₂ of SRFP basically does not show a clearly dependence on either albedo or AOD. We further
 426 investigated the standard deviation of dmXCO₂ by a variation of the bin-to-bin dmXCO₂ with albedo and AOD. dmXCO₂ is
 427 averaged by surface albedo within 0.05 albedo bins and AOD within 0.05 AOD bins, respectively. The standard deviation of
 428 the mean dmXCO₂ in each 0.05 albedo (AOD) bins, i.e. a measure of the bin-to-bin dmXCO₂, is calculated. It is found that
 429 the dmXCO₂ for the four algorithms change with both albedo and AOD in bin-to-bin. In the whole study area, the standard
 430 deviation in albedo is the largest for OCFP, up to 0.7 ppm, while that is smaller from ACOS, NIES and SRFP, 0.4 ppm, 0.3
 431 ppm and 0.2 ppm, respectively. The standard deviation of dmXCO₂ in AOD is larger for SRFP (0.5 ppm) than those for

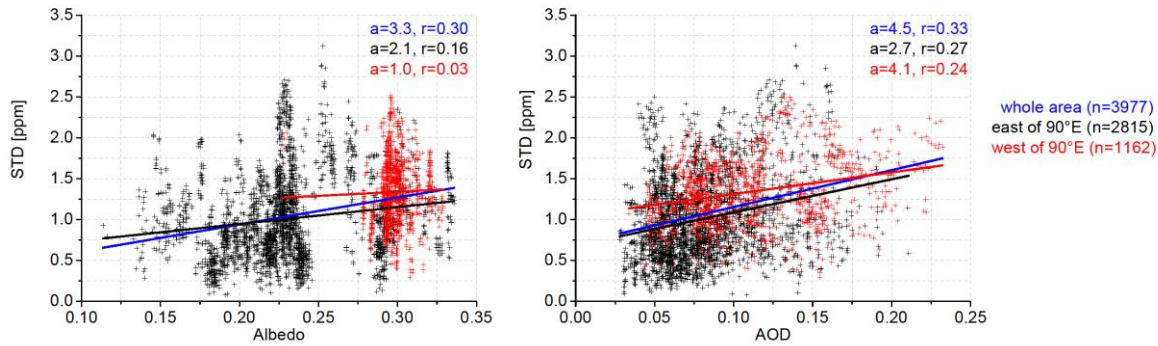
432 ACOS (0.2 ppm), NIES (0.3 ppm) and OCFP (0.4 ppm). Viewing to the deserts (80°E -90°E), the standard deviation in
 433 albedo is the largest from NIES (1.5 ppm), and the smallest from OCFP (0.2 ppm) while they are 1.0 ppm and 0.5 ppm for
 434 ACOS and SRFP, respectively. The standard deviations in AOD, however, are similar (0.2-0.4 ppm) in this area. As a result,
 435 OCFP tend to be more sensitive to albedo and AOD compared to other algorithms. In the deserts, NIES are the most
 436 sensitive XCO₂ retrievals to surface albedo and OCFP the least.



437
 438 Fig. 10: Scatter plots of the differences (dmXCO₂) between GEOS-XCO₂ to ACOS, NIES, OCFP and SRFP respectively, with
 439 respect to albedo (the upper panels) and AOD (the lower panels). Colored points represent the data from different cells: red-[80°E,
 440 105°E], black-[105°E, 120°E] in the study latitude zone [37°N, 42°N]. Colored solid lines display the corresponding linear
 441 regression trend line for the total points. Albedo and AOD are extracted from data products of the retrieval algorithms except
 442 albedo data in OCFP in which GLASS data are used.

443 Figure Fig. 11, moreover, demonstrates the influence of albedo and AOD on the standard deviation (STD) of XCO₂
 444 from four algorithms at the same footprints (timely in the same day, geometrically located within ±0.01° in space).
 445 Averaged albedo (the left panels) and AOD (the right panels) of the four algorithms are used whereas the averaged albedo is
 446 obtained only using three attached albedo in the algorithms except OCFP.

447 The increasing trends of STD with both albedo and AOD can be seen from Fig. 11. The mean STD is 1.3 ppm in the
 448 western cells (80°E -90°E) where albedo is mostly within 0.25-0.35. This STD is lightly larger than that (1.0ppm) in eastern
 449 cells (90°E-120E°) where albedo is comparatively smaller (mostly within 0.15-0.25). It is found from the statistics presented
 450 in Fig. 11 that the correlation coefficients of STD with albedo and that with AOD is almost the same (both are 0.3) for all the
 451 data. Particular influence from albedo in desert over the western cells can be clearly observed. These results indicate that the
 452 inconsistency of XCO₂ retrievals from four algorithms tend to be increase with the enlargements of albedo and AOD so as to
 453 imply that uncertainty of satellite-retrieved XCO₂ should be mostly alerted with the elevations of albedo and AOD.



454

455 **Fig. 11: Scatter plots of the standard deviation (STD) of XCO₂ from the four algorithms to albedo (the left panel) and AOD (the**
 456 **right panel). Colored points represent different cells: red-[80 °E, 105 °E], black-[105 °E, 120 °E] in the latitude zone [37 °N, 42 °N].**
 457 **Colored solid lines display the corresponding linear regression trend line for the scatter plots with the regression slope (a) and the**
 458 **correlation coefficient (r) also presented. n is the number of samples. Albedo is the mean surface albedo in 0.75-um band from the**
 459 **three algorithms including ACOS, NIES and SRFP. AOD is the mean AOD in 0.75-um band from the four algorithms.**

460

461 From the above quantification and analysis in previous sections, the pairwise differences between OCFP and other
 462 algorithms are 0.5+ ppm higher west of 105 °E than east of that, with a difference of 1.2+0.6 ppm over the whole study area.
 463 The obvious regional characteristic probably relates to the assumption of a uniform cirrus profile based on latitude in the
 464 retrieval algorithm (GHG-CCI group at University of Leicester, 2014), which is, however, unlikely to be reasonable in our
 465 study area. There exists a large amount of high clouds over the Tibetan Plateau (Chen et al., 2005), which is located south of
 466 the study cells of 80 °E to 105 °E. The humidity and atmospheric structure are mainly affected by the Tibetan Plateau, and
 467 there is a large difference in the cirrus profile between the western cells and the eastern cells over our study area (Wang et al.,
 468 2012), which indicates that a uniform profile by latitude will inevitably introduce errors.

469 The regional pairwise difference between NIES and other algorithms ~~is 1.6 ppm on average~~, is up to 1.6 ppm, which is
 470 distinctly high among all the algorithms. Considering the complicated geographic environment in the study area, this distinct
 471 difference is likely related to the presumptions from NIES algorithm in aerosol profiles and properties adopted from an
 472 aerosol transport model (Table 1), in which cirrus clouds are ignored and little information from observations is used in the
 473 retrieving process.

474 With the satellite-observed spectrum used for simultaneously retrieving water and clouds, ACOS sets the initial aerosol
 475 types and AOD based on a priori information from aerosol reanalysis data. On the other hand, SRFP handles aerosol based
 476 on a comprehensive characterization of aerosol properties, including aerosol number density, size distribution and aerosol
 477 height. Both of the above two mechanisms function well since ACOS and SRFP are generally demonstrated to provide
 478 relatively better performance.

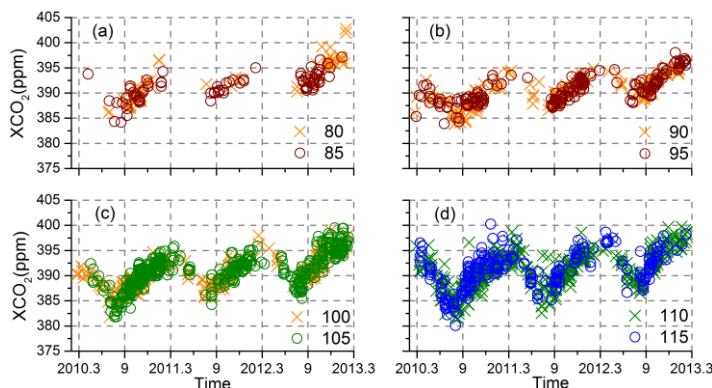
479 Noticing that all algorithms differ in simulating scattering in the atmosphere, such as in the aerosol models, the
 480 influence of scattering on retrieved XCO₂ is too significant to be ignored, as demonstrated from this study. Since satellite
 481 products from different retrieval algorithms in general agree with each other, there is no denying that satellite XCO₂

482 retrievals have the potential to provide more accurate XCO₂ data. Optimization in the handling of aerosol scattering will
483 improve the precision and accuracy of satellite XCO₂ retrievals in the future.

484 5.2 Additional comparison with evaluation of the latest released ACOS V7.3

485 We collected ACOS V7.3 (<http://CO2.jpl.nasa.gov>) too, the latest version of the ACOS data (GES DISC, 2017). We add the
486 cross-comparisons of this version of the data set and other data sets including GEOS-Chem, ACOS V3.5, NIES V02.21,
487 OCFP V6.0 and SRFP V2.3.7 in this section. ACOS V7.3 was created by applying the XCO₂ retrieval algorithms of OCO-2
488 to GOSAT. Within the algorithm code of ACOS V3.5, the OCO-2 algorithm generating ACOS V7.3 data makes some
489 changes in parameter settings, such as the surface pressure a priori constraint and cloud ice properties, and it updates the
490 manners of data processing, for example, the bias corrections and filtering mechanism (GES DISC, 2017).

491 ~~The available data points, a total of 1980, were shown from March 2010 to February 2013 in Fig. 10, where different colors~~
492 ~~and symbols in each panel represent the left longitude of cells into which retrievals fall. In cells west of 90 °E, there are a few~~
493 ~~data points showing abnormal concentrations as high as above 400.0 ppm, which is higher than that of data points in the east,~~
494 ~~where there are strong anthropogenic CO₂ emissions.~~



495 **Fig. 10. The time series of data points from ACOS V7.3 during the period from March 2010 to February 2013. Different symbols**
496 **in each panel represent the left longitude of the cell into which a data point falls.**

498 We made cross-comparisons between ACOS V7.3 and other data sets. No bias was found in ACOS V7.3 from GEOS-Chem
499 with a standard deviation of 1.6 ppm and $R^2=0.77$. The comparison results in the cells are shown in Table 6. Generally,
500 ACOS V7.3 is in good agreement with all of them, which is reflected by correlation coefficients r that are above 0.85 and
501 greater than others, as shown in Table 6. The biggest differences up to 3.0 ppm for ACOS V7.3 are found from NIES and
502 OCFP in deserts cells, whereas differences from SRFP and EMMA are mostly within 1.0 ppm. This is similar to ACOS V3.5.
503 The total absolute difference from other algorithms (not including ACOS V3.5) is within 1.0 ppm in cells east of 110 °E but
504 above 2.0 ppm in cells west of 90 °E. It can also be found from Table 6 that the bias of ACOS V7.3 relative to GEOS-Chem
505 is within 0.3 ppm but above 1.3 ppm, in cells east and west of 90 °E, respectively.

506 Compared to the previous version, ACOS V3.5, ACOS V7.3 increases the average by approximately 0.2 ppm. In
 507 comparison with the difference patterns with ACOS V3.5, the averages of the absolute differences between ACOS V7.3 and
 508 the other four algorithms are similar (<0.1 ppm) and increase by an average of 0.6 ppm (2.1 ppm vs. 1.5 ppm) in cells east of
 509 110 °E and west of 90 °E, respectively, while the biases relative to GEOS-Chem decrease approximately 0.3 ppm and increase
 510 approximately 0.9 ppm in cells east and west of 90 °E, respectively.

511 The comparison results further demonstrate inconsistency of XCO₂ among different datasets in the desert cells.

512 ~~Table 6. Differences between ACOS V7.3 and others (including GEOS-Chem and five other algorithms including ACOS V3.5,~~
 513 ~~NIES, OCFP, SRFP and EMMA) in each cell (subtraction from ACOS V7.3). Values in parentheses are the corresponding~~
 514 ~~standard deviations.~~

Left longitude of cells(°E)	80	85	90	95	100	105	110	115	r
GEOS-Chem	-1.7(1.5) 64	-1.3(1.3) 85	0.1(1.2) 167	0.1(1.2) 191	-0.1(1.3) 294	0.3(1.6) 448	0(1.7) 487	0(1.6) 244	0.88
ACOS V3.5	-0.4(0.9) 103	-0.1(1.0) 48	-0.1(1.0) 133	-0.2(1.0) 189	0.0(1.1) 350	-0.5(1.1) 391	0.2(1.2) 244	-0.1(1.1) 126	0.93
NIES	-3.2(1.2) 61	-1.9(1.5) 100	-1.6(1.2) 251	-1.2(1.9) 123	-1.9(1.4) 541	-1.8(1.5) 317	-1.2(1.6) 397	-0.7(1.5) 277	0.87
OCFP	-3.1(1.0) 66	-3.4(0.9) 41	-2.2(1.1) 157	-2.5(1.5) 114	-2.1(1.2) 297	-1.5(1.1) 329	-0.5(1.1) 396	-0.1(1.0) 202	0.86
SRFP	-0.8(1.3) 138	-0.7(1.4) 145	0.3(1.3) 345	-0.6(1.3) 337	-0.4(1.3) 466	-0.5(1.4) 631	0.3(1.4) 447	0.1(1.2) 247	0.89
EMMA	-0.3(1.3) 113	-0.5(1.4) 90	0.0(1.0) 190	-0.4(1.4) 241	-0.2(1.3) 405	-0.3(1.2) 383	0.3(1.1) 390	0.5(1.1) 233	0.91
Average absolute difference [‡] for four algorithms above	2.2(1.1)	2.0(1.0)	1.4(0.7)	1.7(0.7)	1.6(0.6)	1.4(0.4)	1.1(0.3)	1.0(0.2)	

515 ~~‡ represents the average of absolute differences of ACOS V7.3 matching other algorithms including NIES, OCFP, SRFP and~~
 516 ~~EMMA for each cell.~~

517 6 Conclusion

518 Although TCCON has been widely accepted as the standard for validation of satellite-based XCO₂ data, it is necessary to
 519 better understand the performance of XCO₂ in spatial and timely variations at a regional scale and especially for those
 520 regions where ground-based measurements of XCO₂ are not available, such as for the TCCON stations in China. We
 521 implement the quantification and assessment of the agreement of multiple algorithms for typical regions with various land
 522 covers and enhancement of anthropogenic CO₂ emissions including the megacity of Beijing from 80 °E to 120 °E in the same
 523 latitude band of 40 °N to get better knowledge of the regional uncertainty and performance of GOSAT XCO₂ retrievals in
 524 China. Regional performance of XCO₂ products from four algorithms (ACOS, NIES, OCFP, SRFP) as well as GEOS-Chem

525 simulated XCO₂ are probed to obtain the regional uncertainty and attributions of GOSAT XCO₂ retrievals. In particular, we
 526 apply simulated XCO₂ at a high spatial resolution of 0.5 °(latitude) x 0.666 °(longitude) for a nested grid obtained by GEOS-
 527 Chem to assess the regional uncertainty of XCO₂ derived from satellite observations in China. In connection with the
 528 inconsistency of algorithms in eight cells, the characteristics of aerosol and albedo are investigated to discuss the further
 529 attribution of regional inconsistency of algorithms.

530 Summarizing the performance of four algorithms (ACOS, NIES, OCFP and SRFP) in each cell based on the above
 531 quantification and analysis from comparisons with GEOS-Chem, pairwise differences between algorithms and agreement in
 532 time series among algorithms, we can obtain the following results in general: (1)The consistency among algorithms is better
 533 in the east than in the west as the absolute difference from pairwise comparisons presents ~~0.9-1.5~~0.7-1.1 ppm in eastern cells
 534 covered by grassland, cropland and built-up areas with strong anthropogenic CO₂ emission whereas ~~1.2-2.2~~1.0-1.6 ppm in
 535 western cells covered by desert with a high-brightness surface with less anthropogenic CO₂ emission; (2) ACOS and SRFP
 536 are more satisfying in characterizing spatio-temporal patterns than other algorithms. To conclude, Table 7 presents the
 537 regional characteristics and a summary of the results described in above sections.

538 **Table 7. Summaries of our analyses for uncertainty of XCO₂ retrievals obtained by GOSAT via inter-comparison of multi-**
 539 **algorithms above, including characteristics of regional emissions, albedo, aerosol optical depth, and summary of differences**
 540 **between algorithms and bias compared to GEOS-Chem.**

<u>Characteristics of regions and summary of algorithms</u>		<u>Cells from 80 °E to 115 °E within 37°N-42°N</u>								
<u>Regions</u> <u>Left longitude (°E)</u>		<u>80</u>	<u>85</u>	<u>90</u>	<u>95</u>	<u>100</u>	<u>105</u>	<u>110</u>	<u>115</u>	
<u>Characteristics of regions</u>	<u>CO₂ emissions</u> <u>(Tg/year)*¹</u>	<u>Low emissions</u> <u>(1.2-57.1)</u>					<u>High emissions</u> <u>(515.2-821.9)</u>			
	<u>Property of aerosol</u> <u>(AOD)*²</u>	<u>Dust</u> <u>(0.22-0.53)</u>			<u>Clear</u> <u>(0.10-0.28)</u>			<u>Urban</u> <u>(0.10-0.37))</u>		
	<u>Surface types</u> <u>(albedo)</u>	<u>Sand desert with high</u> <u>brightness</u> <u>(0.20-0.26)</u>			<u>Gobi and grassland</u> <u>(0.19-0.22)</u>			<u>Cropland and</u> <u>built-up</u> <u>(0.14-0.17)</u>		
	<u>Consistency of algorithms</u> <u>(pairwise mean absolute</u> <u>differences)</u>	<u>Less Consistency</u> <u>(1.0-1.6 ppm)</u>					<u>Good consistency</u> <u>(0.7-1.1 ppm)</u>			
<u>Summary of uncertainty</u>	<u>Bias compared to</u> <u>GEOS-Chem</u> <u>(bias range)</u>	<u>Large biases</u> <u>(1.2-3.1 ppm)</u>					<u>lesser biases</u> <u>excluding NIES</u> <u>(0.0-0.5 ppm)</u>			
	<u>General performance of</u> <u>algorithms in spatio-</u> <u>temporal patterns of XCO₂</u> <u>compared to GEOS-Chem</u>	<u>ACOS presents the lowest bias (-0.1 ± 1.9 ppm);</u> <u>SRFP is next (-0.2 ± 2.2 ppm)</u> <u>NIES presents the greatest -2.0 ± 2.2 ppm)</u>								
<u>Left longitude of</u> <u>cells (°E)</u>	<u>80</u>	<u>85</u>	<u>90</u>	<u>95</u>	<u>100</u>	<u>105</u>	<u>110</u>	<u>115</u>		

541

CO ₂ emissions (Tg/year) ^{*1}	20.1 (24.1)	11.2 (7.8)	1.2 (2.7)	35.8 (20.7)	57.1 (15.6)	515.2 (199.0)	801.3 (600.3)	821.9 (893.3)	
Surface type	High brightness desert			Gobi desert			Grassland	Cropland and built-up	
Albedo	0.24	0.26	0.23	0.26	0.22	0.24	0.19	0.21	
AOD ^{*2}	0.22	0.53	0.16	0.42	0.12	0.32	0.10	0.29	
Regional Summary in pairwise differences between algorithms	Less Consistency (mean absolute differences 1.2-2.2 ppm) The difference of OCFP is the greatest with most of the other algorithms (1.7-2.2 ppm); next is NIES (1.6-2.2 ppm).						Good consistency (mean absolute differences 0.9-1.5 ppm) ACOS is relatively the least (0.9-1.1 ppm)		
Regional Summary compared to GEOS-Chem	Large biases, of which NIES is the greatest (1.4-3.1 ppm) and next is OCFP (1.2-2.2 ppm)						lesser biases (0.0-0.5 ppm) excluding NIES		
	Similar in seasonal amplitude;						Seasonal amplitude from GEOS-Chem is lower than all of satellite retrieval algorithms.		
Regional pairwise comparisons of ACOS V7.3	Greater biases are presented with OCFP (1.5-3.4 ppm) and NIES (1.2-3.2 ppm)						Lesser biases (0.0-0.5 ppm) excluding NIES		
General differences compared to GEOS-Chem	ACOS presents lowest values (bias -0.1 ppm Std ^{*3} 1.9 ppm), next is SRFP (bias -0.2 ppm Std 2.2 ppm) NIES presents the greatest (bias 2.0 ppm, Std 2.2 ppm).								
Spatio-temporal patterns of XCO ₂ compared to GEOS-Chem	ACOS and SRFP are similar to GEOS-Chem. OCFP is in better agreement with GEOS-Chem but the bias is larger.								

542 *¹ represents the total emissions of CO₂ from CHRED in each cell in 2012. *² is the range of averaged seasonal aerosol
543 optical depth over a year.

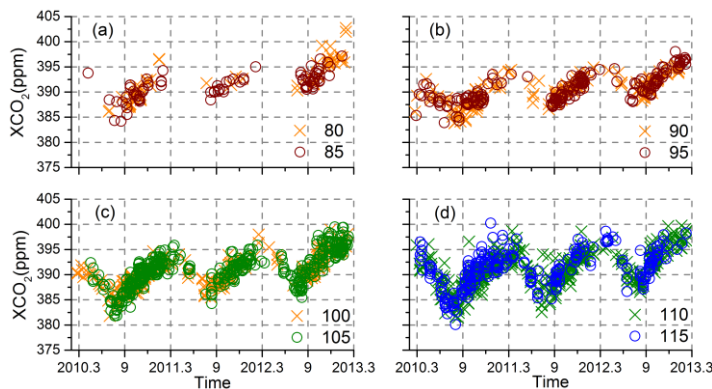
544

545 The results of our analysis, indicating that the discrepancies among algorithms are the smallest in eastern cells which
546 are the strongest anthropogenic emitting source regions in China, implies that the uncertainty of XCO₂ is likely low in this
547 area. It will be sufficiently rigorous for supporting us to apply GOSAT XCO₂ data in assessment of anthropogenic emissions
548 via timely changing magnitude of XCO₂ in such region. Moreover, it was likely that uncertainty in satellite-retrieved XCO₂
549 is attributed to the combined effects of aerosol and albedo. The large uncertainty of XCO₂ must be improved further, even
550 though many algorithms have endeavored to minimize the effects of aerosol and albedo. With the launch of OCO-2 in 2014
551 and GOSAT-2 scheduled for 2018, the prospect of a large amount of useful retrieved XCO₂ products is promising. Since low
552 regional XCO₂ biases are necessary for accurately estimating regional carbon sources and sinks, regional uncertainty should
553 be paid more attention in the future.

554 **Appendix A**

555 We made cross-comparisons between ACOS V7.3 and other data sets. The available data points of ACOS V7.3 were shown
 556 from March 2010 to February 2013 in Fig.S1. In cells west of 90 °E, there are a few data points showing abnormal
 557 concentrations as high as above 400.0 ppm, which is higher than that of data points in the east, where there are strong
 558 anthropogenic CO₂ emissions.

559 The comparison results in the cells are shown in Table S1. No bias was found in ACOS V7.3 from GEOS-Chem with a
 560 standard deviation of 1.6 ppm and R² of 0.77 in the whole study area. Generally, ACOS V7.3 is in good agreement with all
 561 of them, which is reflected by correlation coefficients r that are above 0.85 and greater than others, as shown in Table S1.
 562 The biggest differences up to 3.0 ppm for ACOS V7.3 are found from NIES and OCFP in deserts cells, whereas differences
 563 from SRFP are mostly within 1.0 ppm. This is similar to ACOS V3.5. The pairwise differences from other algorithms (not
 564 including ACOS V3.5) are up to 1.9 ppm in cells west of 90 °E, which is distinctly high, whereas within 0.9 ppm in cells east
 565 of 110 °E. It can also be found that the bias of ACOS V7.3 relative to GEOS-Chem is within 0.3 ppm but above 1.3 ppm, in
 566 cells east and west of 90 °E, respectively.



567
 568 **Fig. S1. The time series of data points from ACOS V7.3 during the period from March 2010 to February 2013. Different symbols**
 569 **in each panel represent the left longitude of the cell into which a data point falls.**

570 **Table S1. Differences between ACOS V7.3 and others (including GEOS-Chem and four other algorithms including ACOS V3.5,**
 571 **NIES, OCFP and SRFP) in each cell (subtraction from ACOS V7.3). Values in parentheses are the corresponding standard**
 572 **deviations.**

<u>Left longitude of cells(°E)</u>	<u>80</u>	<u>85</u>	<u>90</u>	<u>95</u>	<u>100</u>	<u>105</u>	<u>110</u>	<u>115</u>	<u>r</u>
<u>GEOS-Chem</u>	<u>-1.7(1.5)</u> 64	<u>-1.3(1.3)</u> 85	<u>0.1(1.2)</u> 167	<u>0.1(1.2)</u> 191	<u>-0.1(1.3)</u> 294	<u>0.3(1.6)</u> 448	<u>0(1.7)</u> 487	<u>0(1.6)</u> 244	<u>0.88</u>
<u>ACOS V3.5</u>	<u>-0.4(0.9)</u> 103	<u>-0.1(1.0)</u> 48	<u>-0.1(1.0)</u> 133	<u>-0.2(1.0)</u> 189	<u>0.0(1.1)</u> 350	<u>-0.5(1.1)</u> 391	<u>0.2(1.2)</u> 244	<u>-0.1(1.1)</u> 126	<u>0.93</u>
<u>NIES</u>	<u>-3.2(1.2)</u> 61	<u>-1.9(1.5)</u> 100	<u>-1.6(1.2)</u> 251	<u>-1.2(1.9)</u> 123	<u>-1.9(1.4)</u> 541	<u>-1.8(1.5)</u> 317	<u>-1.2(1.6)</u> 397	<u>-0.7(1.5)</u> 277	<u>0.87</u>
<u>OCFP</u>	<u>-3.1(1.0)</u>	<u>-3.4(0.9)</u>	<u>-2.2(1.1)</u>	<u>-2.5(1.5)</u>	<u>-2.1(1.2)</u>	<u>-1.5(1.1)</u>	<u>-0.5(1.1)</u>	<u>-0.1(1.0)</u>	<u>0.86</u>

	<u>66</u>	<u>41</u>	<u>157</u>	<u>114</u>	<u>297</u>	<u>329</u>	<u>396</u>	<u>202</u>	
<u>SRFP</u>	<u>-0.8(1.3)</u>	<u>-0.7(1.4)</u>	<u>0.3(1.3)</u>	<u>-0.6(1.3)</u>	<u>-0.4(1.3)</u>	<u>-0.5(1.4)</u>	<u>0.3(1.4)</u>	<u>0.1(1.2)</u>	<u>0.89</u>
	<u>138</u>	<u>145</u>	<u>345</u>	<u>337</u>	<u>466</u>	<u>631</u>	<u>447</u>	<u>247</u>	
<u>Average absolute difference¹ for three algorithms above</u>	<u>1.9(1.5)</u>	<u>1.7(1.4)</u>	<u>1.2(1.0)</u>	<u>1.4(1.1)</u>	<u>1.3(1.0)</u>	<u>1.2(0.8)</u>	<u>0.9(0.7)</u>	<u>0.7(0.5)</u>	

573 *¹ represents the average of absolute differences of ACOS V7.3 matching other algorithms including NIES, OCFP and SRFP for
574 each cell.

575

576

577 Acknowledgements: This research was supported by the National Research Program on Global Changes and Adaptation:
578 “Big data on global changes: data sharing platform and recognition” (Grant No. 2016YFA0600303, 2016YFA0600304). We
579 are grateful for NIES products from NIES GOSAT Project, albedo data from Beijing Normal University, XCO₂ data from
580 the TCCON data archive, operated by the California Institute of Technology, and supports from GEOS-Chem team. ACOS
581 V3.5 and ACOS V7.3 were produced by the ACOS/OCO-2 project at the Jet Propulsion Laboratory, California Institute of
582 Technology, and obtained from the JPL website, <http://CO2.jpl.nasa.gov> . We are grateful for aerosol data from Aeronautics
583 and Space Administration (NASA). The satellite XCO₂ products OCFP and SRFP have been obtained from the ESA project
584 GHG-CCI website (<http://www.esa-ghg-cci.org/>) and the data providers Univ. Leicester (OCFP product) and SRON & KIT
585 (SRFP) have granted permission to use these data for peer-reviewed publications.

586 References

587 Andres, R. J., Boden, T. A., Br on, F. M., Ciais, P., Davis, S., Erickson, D., Gregg, J. S., Jacobson, A., Marland, G., Miller,
588 J., Oda, T., Olivier, J. G. J., Raupach, M. R., Rayner, P., and Treanton, K.: A synthesis of carbon dioxide emissions from
589 fossil-fuel combustion, Biogeosciences, 9, 1845-1871, <https://doi.org/10.5194/bg-9-1845-2012>, 2012.

590 Bie, N., Lei, L., He, Z., and Liu, M.: An analysis of atmospheric CO₂ concentration around the takelamagan desert with five
591 products retrieved from satellite observations, International Geoscience and Remote Sensing Symposium (IGARSS), Beijing,
592 China, 10-15 July 2016, <https://doi.org/10.1109/IGARSS.2016.7730064>, 2016.

593 Blumenstock, T., Hase, F., Schneider, M., Garcia, O. E. and Sepulveda, E.: TCCON data from Izana, Tenerife, Spain,
594 Release GGG2014R0, TCCON data archive, CDIAC, <https://doi.org/10.14291/tcon.ggg2014.izana01.R0/1149295>, 2014.

595 Bovensmann, H., Burrows, J. P., Buchwitz, M., Frerick, J., No , S., Rozanov, V. V., Chance, K. V., and Goede, A. P. H.:
596 SCIAMACHY: Mission Objectives and Measurement Modes, J. Atmos. Sci., 56, 127-150, 1999.

597 Buchwitz, M., Reuter, M., Schneising, O., Boesch, H., Guerlet, S., Dils, B., Aben, I., Armante, R., Bergamaschi, P.,
598 Blumenstock, T., Bovensmann, H., Brunner, D., Buchmann, B., Burrows, J. P., Butz, A., Ch din, A., Chevallier, F.,

599 Crevoisier, C. D., Deutscher, N. M., Frankenberg, C., Hase, F., Hasekamp, O. P., Heymann, J., Kaminski, T., Laeng, A.,
600 Lichtenberg, G., De Mazière, M., Nođ, S., Notholt, J., Orphal, J., Popp, C., Parker, R., Scholze, M., Sussmann, R., Stiller, G.
601 P., Warneke, T., Zehner, C., Bril, A., Crisp, D., Griffith, D. W. T., Kuze, A., O'Dell, C., Oshchepkov, S., Sherlock, V., Suto,
602 H., Wennberg, P., Wunch, D., Yokota, T., and Yoshida, Y.: The Greenhouse Gas Climate Change Initiative (GHG-CCI):
603 Comparison and quality assessment of near-surface-sensitive satellite-derived CO₂ and CH₄ global data sets, *Remote Sens.*
604 *Environ.*, 162, 344-362, <http://dx.doi.org/10.1016/j.rse.2013.04.024> , 2015.

605 Burrows, J. P., Hölzle, E., Goede, A. P. H., Visser, H., and Fricke, W.: SCIAMACHY—scanning imaging absorption
606 spectrometer for atmospheric cartography, *Acta Astronaut.*, 35, 445-451, [https://doi.org/10.1016/0094-5765\(94\)00278-T](https://doi.org/10.1016/0094-5765(94)00278-T) ,
607 1995.

608 Butz, A., Guerlet, S., Hasekamp, O., Schepers, D., Galli, A., Aben, I., Frankenberg, C., Hartmann, J. M., Tran, H., Kuze, A.,
609 Keppel-Aleks, G., Toon, G., Wunch, D., Wennberg, P., Deutscher, N., Griffith, D., Macatangay, R., Messerschmidt, J.,
610 Notholt, J., and Warneke, T.: Toward accurate CO₂ and CH₄ observations from GOSAT, *Geophys. Res. Lett.*, 38, n/a-n/a,
611 <https://doi.org/10.1029/2011gl047888> , 2011.

612 Cai, B., and Zhang, L.: Urban CO₂ emissions in China: Spatial boundary and performance comparison, *Energy Policy*, 66,
613 557-567, <https://doi.org/10.1016/j.enpol.2013.10.072> , 2014.

614 Chen, B.: Seasonal migration of cirrus clouds over the Asian Monsoon regions and the Tibetan Plateau measured from
615 MODIS/Terra, *Geophys. Res. Lett.*, 32, <https://doi.org/10.1029/2004gl020868>, 2005.

616 Ciais, P., Rayner, P., Chevallier, F., Bousquet, P., Logan, M., Peylin, P., and Ramonet, M.: Atmospheric inversions for
617 estimating CO₂ fluxes: methods and perspectives, *Climatic Change*, 103, 69-92, <https://doi.org/10.1007/s10584-010-9909-3>,
618 2010.

619 Cogan, A. J., Boesch, H., Parker, R. J., Feng, L., Palmer, P. I., Blavier, J. F. L., Deutscher, N. M., Macatangay, R., Notholt,
620 J., Roehl, C., Warneke, T., and Wunch, D.: Atmospheric carbon dioxide retrieved from the Greenhouse gases Observing
621 SATellite (GOSAT): Comparison with ground-based TCCON observations and GEOS-Chem model calculations, *J.*
622 *Geophys. Res. Atmos.*, 117, n/a-n/a, <https://doi.org/10.1029/2012jd018087>, 2012.

623 Connor, B. J., Boesch, H., Toon, G., Sen, B., Miller, C., and Crisp, D.: Orbiting Carbon Observatory: Inverse method and
624 prospective error analysis, *J. Geophys. Res. Atmos.*, 113, n/a-n/a, <https://doi.org/10.1029/2006jd008336>, 2008.

625 Detmers, R., Hasekamp, O.: Product User Guide (PUG) for the RemoTeC XCO₂ Full Physics GOSAT Data Product,
626 available at http://www.esa-ghg-cci.org/sites/default/files/documents/public/documents/GHG-CCI_DATA.html, 2015.

627 Deutscher, N., Notholt, J., Messerschmidt, J., Weinzierl, C., Warneke, T., Petri, C., Grupe, P. and Katrynski, K.: TCCON
628 data from Bialystok, Poland, Release GGG2014R1, TCCON data archive, CDIAC,
629 <https://doi.org/10.14291/tccon.ggg2014.bialystok01.R1/1183984>, 2014.

630 GHG-CCI group at University of Leicester: Algorithm Theoretical Basis Document Version 3 (ATBDv3)-The University of
631 Leicester Full-Physics Retrieval Algorithm for the retrieval of XCO₂ and XCH₄, available at http://www.esa-ghg-cci.org/sites/default/files/documents/public/documents/GHG-CCI_DATA.html, 2014.

632

633 Giglio, L., Randerson, J. T., and van der Werf, G. R.: Analysis of daily, monthly, and annual burned area using the fourth-
634 generation global fire emissions database (GFED4), *J. Geophys. Res. Biogeosci.*, 118, 317-328,
635 <https://doi.org/10.1002/jgrg.20042>, 2013.

636 Graven, H. D., Keeling, R. F., Piper, S. C., Patra, P. K., Stephens, B. B., Wofsy, S. C., Welp, L. R., Sweeney, C., Tans, P. P.,
637 Kelley, J. J., Daube, B. C., Kort, E. A., Santoni, G. W., and Bent, J. D.: Enhanced seasonal exchange of CO₂ by northern
638 ecosystems since 1960, *Science*, 341, 1085-1089, <https://doi.org/10.1126/science.1239207>, 2013.

639 Griffith, D. W. T., Deutscher, N., Velazco, V. A., Wennberg, P. O., Yavin, Y., Aleks, G. K., Washenfelder, R., Toon, G. C.,
640 Blavier, J. F., Murphy, C., Jones, N., Kettlewell, G., Connor, B., Macatangay, R., Roehl, C., Ryzcek, M., Glowacki, J.,
641 Culgan, T. and Bryant, G.: TCCON data from Darwin, Australia, Release GGG2014R0, TCCON data archive, CDIAC,
642 <https://doi.org/10.14291/tcon.ggg2014.darwin01.R0/1149290>, 2014a.

643 Griffith, D. W. T., Velazco, V. A., Deutscher, N., Murphy, C., Jones, N., Wilson, S., Macatangay, R., Kettlewell, G.,
644 Buchholz, R. R. and Riggenschach, M.: TCCON data from Wollongong, Australia, Release GGG2014R0, TCCON data
645 archive, CDIAC, <https://doi.org/10.14291/tcon.ggg2014.wollongong01.R0/1149291>, 2014b.

646 Goddard Earth Science Data Information and Services Center: ACOS Level 2 Standard Product Data User's Guide, v3.5,
647 available at <http://co2.jpl.nasa.gov>, 2016.

648 Goddard Earth Science Data Information and Services Center: ACOS Level 2 Standard Product Data User's Guide, v7.3,
649 available at <http://co2.jpl.nasa.gov>, 2017.

650 Guan, D., Liu, Z., Geng, Y., Lindner, S., and Hubacek, K.: The gigatonne gap in China's carbon dioxide inventories, *Nature*
651 *Clim. Change*, 2, 672-675, <https://doi.org/10.1038/nclimate1560>, 2012.

652 Guerlet, S., Butz, A., Schepers, D., Basu, S., Hasekamp, O. P., Kuze, A., Yokota, T., Blavier, J. F., Deutscher, N. M.,
653 Griffith, D. W. T., Hase, F., Kyro, E., Morino, I., Sherlock, V., Sussmann, R., Galli, A., and Aben, I.: Impact of aerosol and
654 thin cirrus on retrieving and validating XCO₂ from GOSAT shortwave infrared measurements, *J. Geophys. Res. Atmos.*, 118,
655 4887-4905, <https://doi.org/10.1002/jgrd.50332>, 2013.

656 Hase, F., Blumenstock, T., Dohe, S., Gross, J. and Kiel, M.: TCCON data from Karlsruhe, Germany, Release GGG2014R1,
657 TCCON data archive, CDIAC, <https://doi.org/10.14291/tcon.ggg2014.karlsruhe01.R1/1182416>, 2014.

658 Hasekamp, O., Hu, H., Detmers, R., and Butz, A.: ESA Climate Change Initiative (CCI) Algorithm Theoretical Basis
659 Document for the RemoTeC XCO₂ and XCH₄ Full Physics Products of the Essential Climate Variable (ECV) Greenhouse

660 Gases (GHG), available at <http://www.esa-ghg-cci.org/sites/default/files/documents/public/documents/GHG->
661 [CCI_DATA.html](http://www.esa-ghg-cci.org/sites/default/files/documents/public/documents/GHG-CCI_DATA.html), 2015.

662 He, Z., Zeng, Z.-C., Lei, L., Bie, N., and Yang, S.: A Data-Driven Assessment of Biosphere-Atmosphere Interaction Impact
663 on Seasonal Cycle Patterns of XCO₂ Using GOSAT and MODIS Observations, *Remote Sens.*, 9, 251,
664 <https://doi.org/10.3390/rs9030251>, 2017.

665 Hewson, W.: Product User Guide:University of Leicester full-physics XCO₂ retrieval algorithm for CRDP3 – OCFP v6.0,
666 available at http://www.esa-ghg-cci.org/sites/default/files/documents/public/documents/GHG-CCI_DATA.html, 2016.

667 Kawakami, S., Ohyama, H., Arai, K., Okumura, H., Taura, C., Fukamachi, T. and Sakashita, M.: TCCON data from Saga,
668 Japan, Release GGG2014R0, TCCON data archive, CDIAC, <https://doi.org/10.14291/tcon.ggg2014.saga01.R0/1149283>,
669 2014.

670 Keeling, C. D., Bacastow, R. B., Bainbridge, A. E., Ekdahl Jr., C. A., Guenther, P. R., Waterman, L. S., and Chin, J. F. S.:
671 Atmospheric carbon dioxide variations at Mauna Loa Observatory, Hawaii, *Tellus A*, 28,
672 <https://doi.org/10.3402/tellusa.v28i6.11322>, 2011.

673 Keller, C. A., Long, M. S., Yantosca, R. M., Da Silva, A. M., Pawson, S., and Jacob, D. J.: HEMCO v1.0: a versatile,
674 ESMF-compliant component for calculating emissions in atmospheric models, *Geosci. Model Dev.*, 7, 1409-1417,
675 <https://doi.org/10.5194/gmd-7-1409-2014>, 2014.

676 Keppel-Aleks, G., Wennberg, P. O., O'Dell, C. W., and Wunch, D.: Towards constraints on fossil fuel emissions from total
677 column carbon dioxide, *Atmos. Chem. Phys.*, 13, 4349-4357, <https://doi.org/10.5194/acp-13-4349-2013>, 2013.

678 Kivi, R., Heikkinen, P. and Kyro, E.: TCCON data from Sodankyla, Finland, Release GGG2014R0, TCCON data archive,
679 CDIAC, <https://doi.org/10.14291/tcon.ggg2014.sodankyla01.R0/1149280>, 2014.

680 Kulawik, S., Wunch, D., apos, Dell, C., Frankenberg, C., Reuter, M., Oda, T., Chevallier, F., Sherlock, V., Buchwitz, M.,
681 Osterman, G., Miller, C. E., Wennberg, P. O., Griffith, D., Morino, I., Dubey, M. K., Deutscher, N. M., Notholt, J., Hase, F.,
682 Warneke, T., Sussmann, R., Robinson, J., Strong, K., Schneider, M., De Mazi ère, M., Shiomi, K., Feist, D. G., Iraci, L. T.,
683 and Wolf, J.: Consistent evaluation of ACOS-GOSAT, BESD-SCIAMACHY, CarbonTracker, and MACC through
684 comparisons to TCCON, *Atmos. Meas. Tech.*, 9, 683-709, <https://doi.org/10.5194/amt-9-683-2016>, 2016.

685 Lei, H., and Yang, D.: Seasonal and interannual variations in carbon dioxide exchange over a cropland in the North China
686 Plain, *Glob. Chang. Biol.*, 16, 2944-2957, <https://doi.org/10.1111/j.1365-2486.2009.02136.x>, 2010.

687 Lei, L., Guan, X., Zeng, Z., Zhang, B., Ru, F., and Bu, R.: A comparison of atmospheric CO₂ concentration GOSAT-based
688 observations and model simulations, *Sci. Chin.-Earth Sci.*, 57, 1393-1402, <https://doi.org/10.1007/s11430-013-4807-y>, 2014.

689 Lindqvist, H., O'Dell, C. W., Basu, S., Boesch, H., Chevallier, F., Deutscher, N., Feng, L., Fisher, B., Hase, F., Inoue, M.,
690 Kivi, R., Morino, I., Palmer, P. I., Parker, R., Schneider, M., Sussmann, R., and Yoshida, Y.: Does GOSAT capture the true
691 seasonal cycle of carbon dioxide?, *Atmos. Chem. Phys.*, 15, 13023-13040, <https://doi.org/10.5194/acp-15-13023-2015>, 2015.

692 Liu, D., Lei, L., Guo, L., and Zeng, Z.-C.: A Cluster of CO₂ Change Characteristics with GOSAT Observations for Viewing
693 the Spatial Pattern of CO₂ Emission and Absorption, *Atmosphere*, 6, 1695-1713, <https://doi.org/10.3390/atmos6111695>,
694 2015.

695 Liu, Z., Guan, D., Wei, W., Davis, S. J., Ciais, P., Bai, J., Peng, S., Zhang, Q., Hubacek, K., Marland, G., Andres, R. J.,
696 Crawford-Brown, D., Lin, J., Zhao, H., Hong, C., Boden, T. A., Feng, K., Peters, G. P., Xi, F., Liu, J., Li, Y., Zhao, Y., Zeng,
697 N., and He, K.: Reduced carbon emission estimates from fossil fuel combustion and cement production in China, *Nature*,
698 524, 335-338, <https://doi.org/10.1038/nature14677>, 2015.

699 Messerschmidt, J., Parazoo, N., Wunch, D., Deutscher, N. M., Roehl, C., Warneke, T., and Wennberg, P. O.: Evaluation of
700 seasonal atmosphere–biosphere exchange estimations with TCCON measurements, *Atmos. Chem. Phys.*, 13, 5103-5115,
701 <https://doi.org/10.5194/acp-13-5103-2013>, 2013.

702 Morino, I., Matsuzaki, T. and Shishime, A.: TCCON data from Tsukuba, Ibaraki, Japan, 125HR, Release GGG2014R1,
703 TCCON data archive, CDIAC, <https://doi.org/10.14291/tcon.ggg2014.tsukuba02.R1/1241486>, 2014.

704 Nassar, R., Jones, D. B. A., Suntharalingam, P., Chen, J. M., Andres, R. J., Wecht, K. J., Yantosca, R. M., Kulawik, S. S.,
705 Bowman, K. W., Worden, J. R., Machida, T., and Matsueda, H.: Modeling global atmospheric CO₂ with improved emission
706 inventories and CO₂ production from the oxidation of other carbon species, *Geosci. Model Dev.*, 3, 689-716,
707 <https://doi.org/10.5194/gmd-3-689-2010>, 2010.

708 Nassar, R., Napier-Linton, L., Gurney, K. R., Andres, R. J., Oda, T., Vogel, F. R., and Deng, F.: Improving the temporal and
709 spatial distribution of CO₂ emissions from global fossil fuel emission data sets, *J. Geophys. Res. Atmos.*, 118, 917-933,
710 <https://doi.org/10.1029/2012jd018196>, 2013.

711 National Institute for Environmental Studies, GOSAT Project Office: NIES GOSAT TANSO-FTS SWIR Level 2 Data
712 Product Format Description Version 2.50, available at <https://data2.gosat.nies.go.jp/doc/document.html#Document>, 2015.

713 Oda, T., and Maksyutov, S.: A very high-resolution (1 km×1 km) global fossil fuel CO₂ emission inventory derived using a
714 point source database and satellite observations of nighttime lights, *Atmos. Chem. Phys.*, 11, 543-556,
715 <https://doi.org/10.5194/acp-11-543-2011>, 2011.

716 O'Dell, C. W., Connor, B., Bösch, H., O'Brien, D., Frankenberg, C., Castano, R., Christi, M., Eldering, D., Fisher, B.,
717 Gunson, M., McDuffie, J., Miller, C. E., Natraj, V., Oyafuso, F., Polonsky, I., Smyth, M., Taylor, T., Toon, G. C., Wennberg,
718 P. O., and Wunch, D.: The ACOS CO₂ retrieval algorithm – Part 1: Description and validation against synthetic observations,
719 *Atmos. Meas. Tech.*, 5, 99-121, <https://doi.org/10.5194/amt-5-99-2012>, 2012.

720 Oshchepkov, S., Bril, A., Yokota, T., Wennberg, P. O., Deutscher, N. M., Wunch, D., Toon, G. C., Yoshida, Y., O'Dell, C.
721 W., Crisp, D., Miller, C. E., Frankenberg, C., Butz, A., Aben, I., Guerlet, S., Hasekamp, O., Boesch, H., Cogan, A., Parker,
722 R., Griffith, D., Macatangay, R., Notholt, J., Sussmann, R., Rettinger, M., Sherlock, V., Robinson, J., Kyrö, E., Heikkinen, P.,
723 Feist, D. G., Morino, I., Kadyrov, N., Belikov, D., Maksyutov, S., Matsunaga, T., Uchino, O., and Watanabe, H.: Effects of
724 atmospheric light scattering on spectroscopic observations of greenhouse gases from space. Part 2: Algorithm
725 intercomparison in the GOSAT data processing for CO₂ retrievals over TCCON sites, *J. Geophys. Res. Atmos.*, 118, 1493-
726 1512, <https://doi.org/10.1002/jgrd.50146>, 2013.

727 Sherlock, V., Connor, B., Robinson, J., Shiona, H., Smale, D. and Pollard, D.: TCCON data from Lauder, New Zealand,
728 125HR, Release GGG2014R0, TCCON data archive, CDIAC, <https://doi.org/10.14291/tcon.ggg2014.lauder02.R0/1149298>,
729 2014.

730 Sussmann, R. and Rettinger, M.: TCCON data from Garmisch, Germany, Release GGG2014R0, TCCON data archive,
731 CDIAC, <https://doi.org/10.14291/tcon.ggg2014.garmisch01.R0/1149299>, 2014.

732 Takahashi, T., Sutherland, S. C., Wanninkhof, R., Sweeney, C., Feely, R. A., Chipman, D. W., Hales, B., Friederich, G.,
733 Chavez, F., and Sabine, C.: Takahashi, T. et al. Climatological mean and decadal changes in surface ocean pCO₂, and net
734 sea-air CO₂ flux over the global oceans, *Deep-Sea Res. Pt. II*, 56, 554-577, <https://doi.org/10.1016/j.dsr2.2008.12.009>, 2009.

735 Thoning, K. W., Tans, P. P., and Komhyr, W. D.: Atmospheric carbon dioxide at Mauna Loa Observatory: 2. Analysis of the
736 NOAA GMCC data, 1974-1985, *J. Geophys. Res. Atmos.*, 94, 8549-8565, <https://doi.org/10.1029/JD094iD06p08549>, 1989.

737 Wang, J., Cai, B., Zhang, L., Cao, D., Liu, L., Zhou, Y., Zhang, Z., and Xue, W.: High resolution carbon dioxide emission
738 gridded data for China derived from point sources, *Environ. Sci. Technol.*, 48, 7085-7093, <https://doi.org/10.1021/es405369r>,
739 2014.

740 Wang, W., Tian, Y., Liu, C., Sun, Y., Liu, W., Xie, P., Liu, J., Xu, J., Morino, I., Velasco, V. A., Griffith, D. W. T., Notholt,
741 J., and Warneke, T.: Investigating the performance of a greenhouse gas observatory in Hefei, China, *Atmos. Meas. Tech.*, 10,
742 2627-2643, <https://doi.org/10.5194/amt-10-2627-2017>, 2017..

743 Wang Min-zhong, H. Q., Wei Wen-shou, Yang Lian-mei, and Zhao Yong: Observational Analysis of the Troposphere and
744 Low Stratosphere at Minfeng Station in the North Side of the Tibetan Plateau in July 2011, *Plateau Meteorology*, 31, 12,
745 2012.

746 Warneke, T., Messerschmidt, J., Notholt, J., Weinzierl, C., Deutscher, N., Petri, C., Grupe, P., Vuillemin, C., Truong, F.,
747 Schmidt, M., Ramonet, M. and Parmentier, E.: TCCON data from Orleans, France, Release GGG2014R0, TCCON data
748 archive, CDIAC, <https://doi.org/10.14291/tcon.ggg2014.orleans01.R0/1149276>, 2014.

749 Watson, D. F., and Philip, G. M.: Triangle based interpolation, *Mathematical Geology*, 16, 779-795,
750 <https://doi.org/10.1007/BF01036704>, 1984.

751 Wennberg, P. O., Roehl, C., Blavier, J. F., Wunch, D., Landeros, J. and Allen, N.: TCCON data from Jet Propulsion
752 Laboratory, Pasadena, California, USA, Release GGG2014R0, TCCON data archive, CDIAC,
753 <https://doi.org/10.14291/tccon.ggg2014.jpl02.R0/1149297>, 2014a.

754 Wennberg, P. O., Roehl, C., Wunch, D., Toon, G. C., Blavier, J. F., Washenfelder, R., Keppel-Aleks, G., Allen, N. and
755 Ayers, J.: TCCON data from Park Falls, Wisconsin, USA, Release GGG2014R0, TCCON data archive, CDIAC,
756 <https://doi.org/10.14291/tccon.ggg2014.parkfalls01.R0/1149161>, 2014b.

757 Wennberg, P. O., Wunch, D., Roehl, C., Blavier, J. F., Toon, G. C., Allen, N., Dowell, P., Teske, K., Martin, C. and Martin,
758 J.: TCCON data from Lamont, Oklahoma, USA, Release GGG2014R0, TCCON data archive, CDIAC,
759 <https://doi.org/10.14291/tccon.ggg2014.lamont01.R0/1149159>, 2014c.

760 Wunch, D., Wennberg, P. O., Toon, G. C., Connor, B. J., Fisher, B., Osterman, G. B., Frankenberg, C., Mandrake, L., O'Dell,
761 C., Ahonen, P., Biraud, S. C., Castano, R., Cressie, N., Crisp, D., Deutscher, N. M., Eldering, A., Fisher, M. L., Griffith, D.
762 W. T., Gunson, M., Heikkinen, P., Keppel-Aleks, G., Kyr ö E., Lindenmaier, R., Macatangay, R., Mendonca, J.,
763 Messerschmidt, J., Miller, C. E., Morino, I., Notholt, J., Oyafuso, F. A., Rettinger, M., Robinson, J., Roehl, C. M., Salawitch,
764 R. J., Sherlock, V., Strong, K., Sussmann, R., Tanaka, T., Thompson, D. R., Uchino, O., Warneke, T., and Wofsy, S. C.: A
765 method for evaluating bias in global measurements of CO₂ total columns from space, *Atmos. Chem. Phys.*, 11, 12317-12337,
766 <https://doi.org/10.5194/acp-11-12317-2011>, 2011.

767 Yokota, T., Oguma, H., Morino, I., and Inoue, G.: A nadir looking SWIR sensor to monitor CO₂ column density for
768 Japanese GOSAT project, Proceedings of the twenty-fourth international symposium on space technology and science,
769 Miyazaki: Japan Society for Aeronautical and Space Sciences and ISTS, 887-889, 2004.

770 Yoshida, Y., Kikuchi, N., Morino, I., Uchino, O., Oshchepkov, S., Bril, A., Saeki, T., Schutgens, N., Toon, G. C., Wunch, D.,
771 Roehl, C. M., Wennberg, P. O., Griffith, D. W. T., Deutscher, N. M., Warneke, T., Notholt, J., Robinson, J., Sherlock, V.,
772 Connor, B., Rettinger, M., Sussmann, R., Ahonen, P., Heikkinen, P., Kyr ö E., Mendonca, J., Strong, K., Hase, F., Dohe, S.,
773 and Yokota, T.: Improvement of the retrieval algorithm for GOSAT SWIR XCO₂ and XCH₄ and their validation using
774 TCCON data, *Atmos. Meas. Tech.*, 6, 1533-1547, <https://doi.org/10.5194/amt-6-1533-2013>, 2013.

775 Zeng, Z.-C., Lei, L., Strong, K., Jones, D. B. A., Guo, L., Liu, M., Deng, F., Deutscher, N. M., Dubey, M. K., Griffith, D. W.
776 T., Hase, F., Henderson, B., Kivi, R., Lindenmaier, R., Morino, I., Notholt, J., Ohyama, H., Petri, C., Sussmann, R., Velazco,
777 V. A., Wennberg, P. O., and Lin, H.: Global land mapping of satellite-observed CO₂ total columns using spatio-temporal
778 geostatistics, *Int. J. Digit. Earth*, 1-31, <https://doi.org/10.1080/17538947.2016.1156777>, 2016.

779 Zhang, X. Y., Wang, Y. Q., Niu, T., Zhang, X. C., Gong, S. L., Zhang, Y. M., and Sun, J. Y.: Atmospheric aerosol
780 compositions in China: spatial/temporal variability, chemical signature, regional haze distribution and comparisons with
781 global aerosols, *Atmos. Chem. Phys.*, 12, 779-799, <https://doi.org/10.5194/acp-12-779-2012>, 2012.